CHALMERS

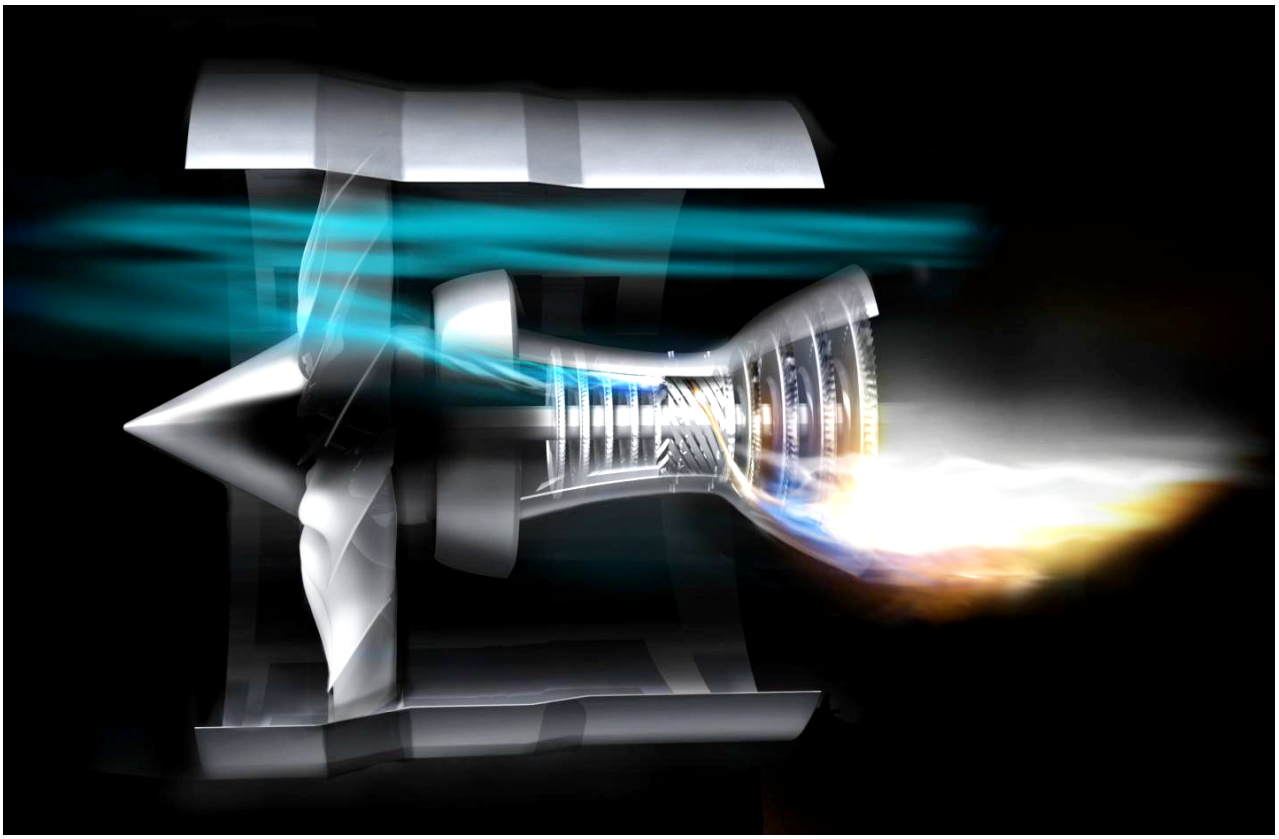

Indirect Combustion Noise: Large Eddy Simulation of a full scale Lab nozzle

Master's thesis in Fluid Mechanics

JUN ZHENG

Department of Applied Mechanics
Division of Fluid Mechanics
CHALMERS UNIVERSITY OF TECHNOLOGY
Gothenburg, Sweden 2012
Master's thesis 2012:44

MASTER'S THESIS IN FLUID MECHANICS

Indirect Combustion Noise: Large Eddy Simulation of a full scale Lab nozzle

JUN ZHENG

Department of Applied Mechanics
Division of Fluid Mechanics
CHALMERS UNIVERSITY OF TECHNOLOGY
Gothenburg, Sweden 2012

Indirect Combustion Noise: Large Eddy Simulation of a full scale Lab nozzle
JUN ZHENG

Master's thesis 2012:44
ISSN 1652-8557
Department of Applied Mechanics
Division of Fluid Mechanics
Chalmers University of Technology
SE-412 96 Gothenburg
Sweden
Telephone: +46 (0)31-772 1000

Cover:
Picture extracted from Tomas Grönstedt presentation ISABE 2011

Chalmers Reproservice
Gothenburg, Sweden 2012

Indirect Combustion Noise: Large Eddy Simulation of a full scale Lab nozzle
Master's thesis in Fluid Mechanics
JUN ZHENG
Department of Applied Mechanics
Division of Fluid Mechanics
Chalmers University of Technology

Abstract

In 1998, the X-Noise collaborative network project was created uniting 32 European partners (companies, universities, institutes). The objective of this project is to reduce the exposure of community to aircraft noise precisely by a factor 2 (-10 dB) in 2020. At the beginning of 2010, a drastic decrease of the aero-acoustic noise by 5dB was reached and led to an increase in the relative contribution of combustion noise. In this report, the nozzle of the test bench located at EM2C Laboratory was studied using the LES 3D solver CEDRE. The description of the combustion noise, which can be divided into direct and indirect noise, and the methods used for its prediction and its analyse will be explained. Then the DISCERN project will be detailed. After that the numerical simulation of the nozzle will be performed. The acoustic transfer functions of the system will then be calculated using the CEDRE code. But due to time constraints, the calculation has been fully performed on a coarse mesh and the analysis of the results from the fine mesh is still under way. For the coarse mesh, the acoustic transfer functions seems to be much higher than the results from the analytical MARCAN solver. The first hypothesis might be the creation of a jet in the divergent part of the nozzle. This jet leads to an uncontrolled and undesired acoustic disturbances. As a conclusion, the geometry has to be changed, the angle of the divergent part should be decreased to avoid the detached flow. Under this condition, the study of the acoustic noise generated by the injection of entropy fluctuation will be more accurate.

Keywords: Combustion Noise, Direct, Indirect, Large Eddy Simulation, Acoustic, Nozzle, Entropy fluctuations

Acknowledgements

First of all I would like to begin with my supervisor Alexis Giauque. Alexis, thank you for welcoming me in Acoustic unity, giving me the opportunity to work in the aerospace field and supporting me everyday during this internship. Your writing skills for the corrections of my report was really helpful. Also your interest and your enthusiasm throughout the internship, helped me to go on day by day. I am really happy to work with you during the next three years of a PhD.

In addition, I would like to thank Maxime Huet for his help and his advices during this six months length internship. I have met a lot of people inside the work sphere especially in Acoustic unity but also in the Computational Fluid Dynamics and Aeroacoustics (DSNA). Whether you are an engineer, a searcher, a PhD student or just a Master student like me, I would like to say thank you to all of you for your help, your jollity and your care.

Nomenclature

c	Fluid mean sound speed
C_p	Heat capacity at constant pressure
f	Frequency
$f^{'}$	Fluctuating frequency
M	Mach number
m	Mass flow rate
p	Fluid pressure
$p^{'}$	Fluctuating fluid pressure
s	Fluid entropy
$s^{'}$	Fluctuating fluid entropy
t	Time
T	Temperature
T'	Fluctuating temperature
W	Work
T_t	Fluid total temperature
u	Fluid velocity
u'	Fluctuating fluid velocity
u^+	Fluid velocity downstream
u^-	Fluid velocity upstream
P^+	Acoustic wave propagating downstream
P^-	Acoustic wave propagating upstream
P_1	Acoustic wave for the inlet flow
P_2	Acoustic wave for the outlet flow
P_3	Acoustic wave downstream to the shock
x	Axial coordinate of the nozzle
A	Surface
r	Specific gas constant
grad	gradient
rot	rotational
Δt	Time step of the numerical simulation
γ	Specific heats ratio
λ	Characteristic acoustic wavelength
σ	Entropy wave
ρ	Density
$\rho^{'}$	Fluctuating fluid mean density
Ω_{ij}	antisymmetric part of the gradient of u
S_{ij}	symmetric part of the gradient of u
Q	Second invariant of the gradient of u

Contents

List of Figures

List of Tables

Introduction

Complex flow and especially turbulent combustion can produce acoustic, entropic or vorticity waves. Regardless of the type of noise considered, those waves are propagated though the system. This report will first sum up the different tools used in noise prediction and characterisation of combustion noise. Several methods for the prediction of this type of acoustic disturbance can be used (for example analytical, experimental or numerical approach) and will also be explained. During the 70's, two mechanisms have been identified as combustion noise.

- Direct noise is generated by unsteady heat release rate at the flame front level. This noise appears in unsteady combustion situations, in opened or confined configurations. This acoustic disturbance has been extensively investigated from theoretical, numerical and experimental points of view. In laminar configuration, the driving mechanisms are now well known. But recently intense efforts have been carried out to investigate turbulent confined situations.

- Indirect noise was theoretically predicted and observed experimentally during the same period of time. This noise is induced by the acceleration of burnt gas heterogeneities both in velocity (vorticity) and temperature (entropy waves).

Initial measurements and theoretical works tend to show that the levels of noise due to indirect and direct mechanisms are of the same order of magnitude. And it appears to be crucial to study those two phenomena more in details and to precisely discern their respective contribution to combustion noise. In spite of the numerous studies conducted during the past thirty years it is still a challenging issue to isolate direct from indirect noise sources. This is mainly due to the very limited means of measurement, the extreme operating conditions (high pressure and temperature gradients) and also the complex physical processes (chemical reactions and variable Mach number flows). This leads to very high constraints on the numerical methods as well as on the experimental means and diagnostics for the investigation of core noise under real engine conditions. Finally, it has been showed that acoustic pressure and velocity amplitudes are at least two orders of magnitude lower than the aerodynamic values encountered in the systems, requiring extremely clean and sensitive computations and measurements.

This report will first describe ONERA then an overall view of Combustion noise will be given. In addition the context of the internship linked with the DISCERN project will be presented. After that, the numerical tools used and the calculations will be developed leading to an analysis part and a results part. Those sections will describe respectively the encountered problems during the internship and some initial results.

1 Presentation of the ONERA

ONERA (Office National d'Etudes et Recherches Aérospatiales) is the French national aerospace research centre. It is a public research establishment financed by the French government (35%) and either industrial contract research (65%) for a total of 227 Millions Euros budget. In fact, the subsidy given by the French government is a long-term research development whereas research contracts for industries or agencies are more for short or medium term projects. With eight major facilities in France (see Figure 1.0.1) and about 2,100 employees, including 1,500 scientists, engineers and technicians, ONERA is leading the edge of the French aerospace research. Since 1946, its mission is to:

- Direct and conduct aeronautical research.
- Support the commercialization of this research by national and European industry.
- Construct and operate the associated experimental facilities.
- Supply industry with high-level technical analyses and other services.
- Perform technical analyses for the government.
- Train researchers and engineers.

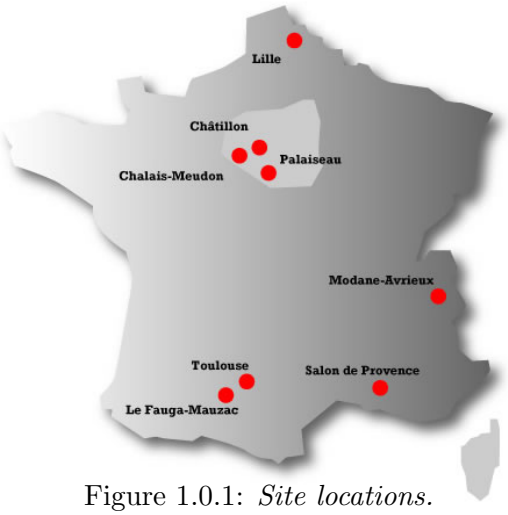

Figure 1.0.1: *Site locations.*

Regarding to those objectives, ONERA has divided his research into 4 scientific branches regrouping 16 departments. See table 1.0.1. This internship will take place in the Computational Fluid Dynamics and Aeroacoustics (DSNA) department, more precisely in the **ACOU** unity. The DSNA is in charge of developing numerical simulation tools and also to perform fluid mechanics or aeroacoustic experimental studies.

All of this research is keyed to applications. Whether the research has short, medium or long-term goals, it is designed to support the competitiveness and creativity of the aerospace and defense industries. The research carried out at ONERA results in computation codes, methods, tools, technologies, materials and other products and services which are used to design and manufacture everything linked with aerospace:

- Civil aircraft.
- Military aircraft.

- Helicopters and tiltrotors.
- Propulsion systems.
- Orbital systems.
- Space transport.
- Missile systems.
- Defence systems.
- Networked systems and security systems.

Hence, ONERA's "business portfolio" is linked with military industries but it has anyway a very balanced with 1/3 for civil, 1/3 for defense and 1/3 for both technology.

 Materials and Structures	Aeroelasticity and Structural Dynamics - DADS Composite Materials and Structures - DMSC Metallic Materials and Structures - DMSM Laboratory for Microstructural Investigations (joint ONERA-CNRS) - LEM
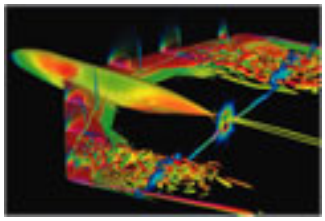 Fluid Mechanics and Energetics	Applied Aerodynamics - DAAP Fundamental and Experimental Aerodynamics - DAFE Fundamental and Applied Energetics - DEFA Aerodynamics and Energetics Modeling - DMAE Computational Fluid Dynamics and Aeroacoustics - DSNA
 Physics	Electromagnetism and Radar - DEMR Space Environment - DESP Physics and Instrumentation - DMPH Theoretical and Applied Optics - DOTA
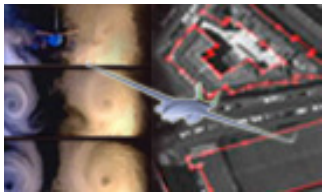 Information Processing and Systems	Systems Control and Flight Dynamics - DCSD System Design and Performance Evaluation - DCPS Modelling and Information Processing - DTIM

Table 1.0.1: Four branches and 16 scientific departments.

2 Combustion noise

Over the past 20 years, substantial progress has been made in order to reduce aircraft noise. Improvements related to the airframe and jet exhausts have been particularly significant. The noise produced by the engine is experiencing a growing interest. During the 70's, Marble and Candel [31] have identified two main different sources of combustion noise. It was also shown during the last decades that combustion instabilities is the major source of acoustic disturbance in a combustion chamber. Two types of noise are described in this report:

- The "direct" combustion noise related to the unsteady heat release fluctuation in the combustion chamber.

- The "indirect" combustion noise, related to the acceleration in a nozzle or a turbine row of temperature or vorticity inhomogeneities created by the flame.

As the internship focuses on the simulation of indirect combustion noise in aero-engines, only this type will be explained in detail in this document. Nevertheless, the direct noise will also be briefly described.

2.1 Direct Noise

First, one can use the analytical approach. But since the combustion is strongly linked with turbulent effects, no general analytical model has been found to describe accurately heat release and noise radiation. One can cite for example, the theoretical studies led by Bragg [10] and Strahle [45] who mainly focused on finding acoustic power or integral formulation of noise radiation near an opened flame. Those formulations use Green's theorem which cannot be used in confined domains due to the complexity of Green's function. Hence, this approach will not be further developed in this document.

2.1.1 Experimental methods

Several experiments have been carried out in order to collect aerodynamic and acoustic measurements, which explain the theoretical aspects of combustion noise. Among those, one can cite Thomas & Williams [46] who describe the development of a flame in an opened field spherical domain through the ignition of a pre-mixed combustible gas in soap bubbles (see the Figure 2.1.1 on the left hand side). The ignition occurs at constant pressure and the volume of the soap bubble increases after ignition. As a consequence, its surface increases and a pressure wave occurs at the interface. Since the bubble size is small compared to the acoustic wavelength, this type of emission can be considered as monopolar. In Figure 2.1.1 on the right hand side, one can see that the measured pressure is close to the computed one.

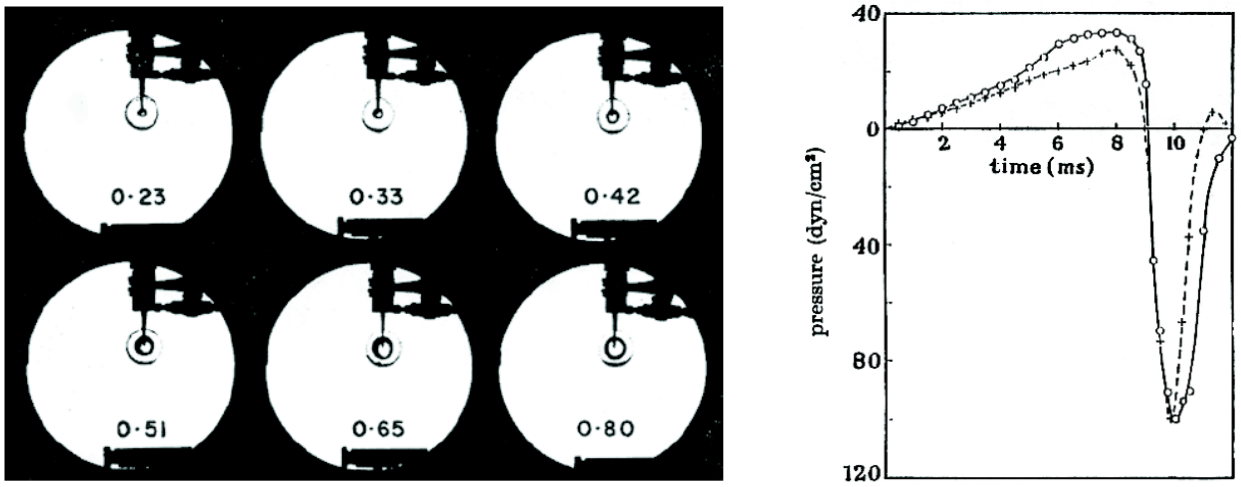

Figure 2.1.1: *Results from Thomas & Williams [46]. left: Instantaneous shots of a spherical expanding flame after ignition over time, right: acoustic pressure produced by an air-ethylene spherical flame, + measured pressure; ∘ computed pressure.*

Direct measurement of combustion noise in chambers are less common. The ONERA (The French Aerospace Lab) and DLR (Deutsches Zentrum für Luft- und Raumfahrt) for example, have combustion chamber facilities in which one can measure the direct noise. Lamraoui [26] at EMC2 laboratory from Ecole Centrale Paris developed a combustion test chamber with the noteworthy possibility to change the downstream boundary condition (opened field outflow or accelerated outflow through a nozzle).

2.1.2 Numerical methods

Numerical methods with different degrees of complexity can be used to determine sound emission from direct combustion. Indeed, with technical progress, it is now possible to simulate the behaviour of full aero-engines. Candel *et* al. [11] give a nice summary of the different numerical methods available. They list three main techniques, the stochastic method, the statistical method and the unsteady aerodynamic simulations. The first technique is not really used since a reasonable unsteady fluctuating field is needed, the construction of such a field being hard. The statistical technique is experiencing a growing interest in the scientific community thanks to its low cost. LES (Large Eddy Simulation) and DNS (Direct Numerical Simulation) belong to the last category and the flame description obtained from such methods is detailed and matches the reality well.

2.2 Indirect Noise

The indirect combustion noise is related to the acceleration in a nozzle or a turbine stage of temperature or vorticity inhomogeneities in a flow with a non zero pressure gradient. Due to the density fluctuation associated to the inhomogeneity, the acceleration of this disturbance is different from the rest of the flow. Thus, the flow returns to its equilibrium by the generating an acoustic wavefront. This wavefront is responsible of the indirect noise. Different methods for generating and modelling of this kind of noise are presented in the following sections. Yet, those methods are different depending on whether the flow is accelerated through a nozzle or a turbine and thus this section will be separated in two parts.

2.2.1 Flow passing a nozzle

Experimental method

The ONERA or the DLR have combustion chamber setups but DLR only hosts the EWG (Entropy Wave Generator) facility. Such configurations are shown in Figure 2.2.1. Bake *et* al. [3] found that in the combustion chamber setup, indirect noise is the upstream dominating source of combustion noise. In addition, using the EWG, they also showed that entropy spots convected through the nozzle generate large quantity of noise. The main difference between generic combustion chambers and the EWG is that in the EWG one can measure the indirect combustion noise independently whereas in generic combustion chambers one cannot separate the contributions of both direct and indirect noise. As one can see in Figure 2.2.2, numerical simulation gives almost the same results as the measured one.

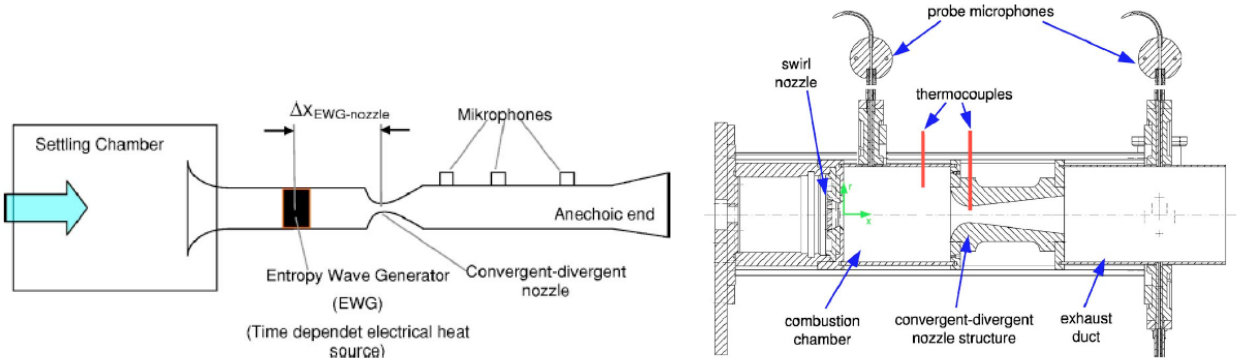

Figure 2.2.1: *Sketches of the Entropy Wave Generator (left) and the combustion chamber setup (right) from Bake et al. [3].*

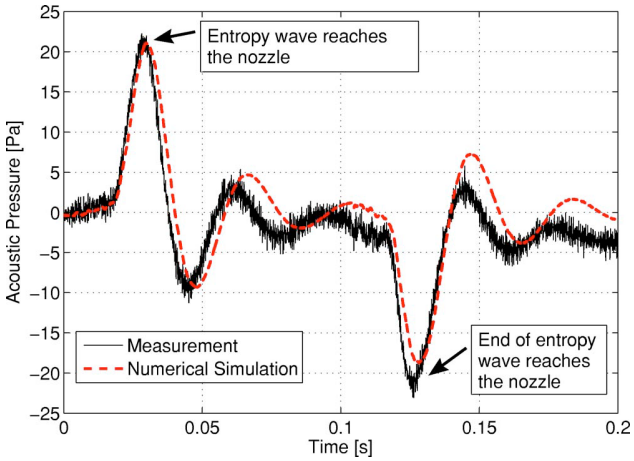

Figure 2.2.2: *Comparison data between computed and measured values from from Bake et al. [3].*

A VGW (Vorticity Wave Generator) has also been built at DLR. This setup has been used by N. Kings *et* al. [5] and is sketched in Figure 2.2.3. The only difference between the VWG and the EWG is that the perturbation generation area is different. In the VWG, vortices are generated through the injection of pressurized air in the azimuthal direction. N. Kings *et* al. [5] have shown that accelerated vortices passing in a nozzle generate pressure fluctuations. According to their experiments, for a fixed Mach number, increasing the mass flow of the carrying phase augments both, vortex noise amplitude

and vorticity see Figure 2.2.4.

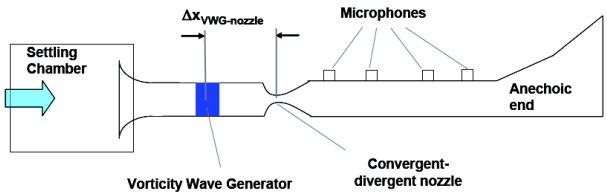

Figure 2.2.3: *Sketch of the Vorticity Wave Generator.*

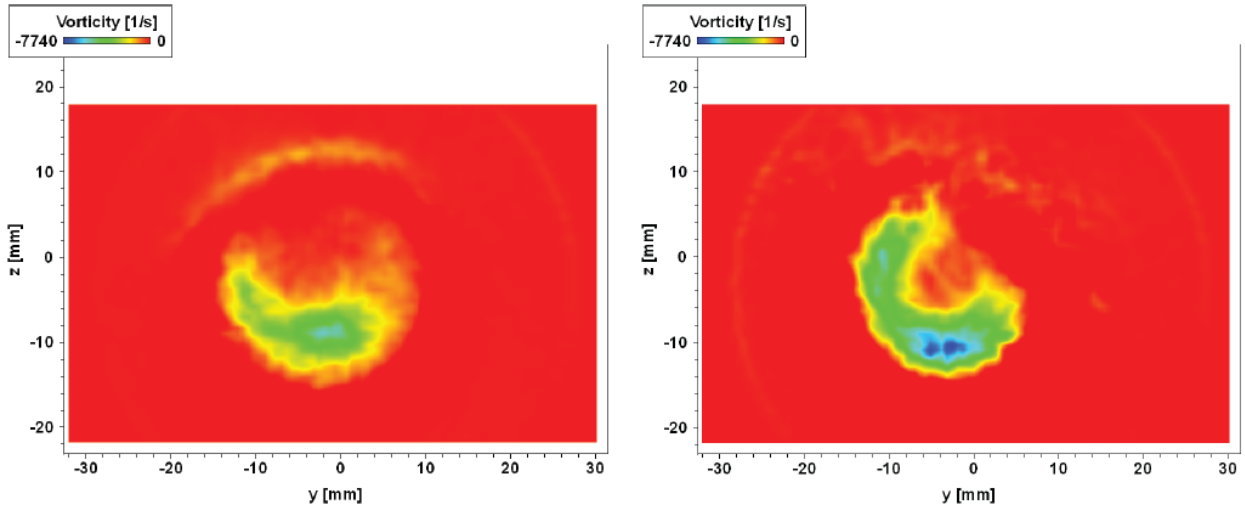

Figure 2.2.4: *Vorticity fields; left hand side: low air-injection 0.55*kg/h*, right hand side: high air-injection 1.1*kg/h.

Analytical method

Marble & Candel [31] did the first analytical investigation on indirect noise generated by the passage in a nozzle of an acoustic or an entropic wave. They simplify the problem by assuming a compact nozzle in the subsonic domain and extend the model to a non conpact nozzle in the supersonic limit. The compact nozzle hypothesis is only valid at low frequency for which wavelengths are large compared to the nozzle size. Their compact model is based on the following assumptions:

- One dimensional flow (axial flow).
- No viscous effects (Euler equation).
- Perfect gas (constant γ).
- Equations can be linearised (small fluctuations).
- Compact nozzle compared to acoustic wavelength for subsonic cases.

One can question whether the three last hypothesis are relevant during the combustion process in reality. This idea was already studied by Leyko [29] and others.

Marble & Candel [31] based their method on conservation equations which are provided below. Some derivations are given in the Appendix A:

$$\frac{1}{\rho}\left(\frac{\partial \rho}{\partial t} + u\frac{\partial \rho}{\partial x}\right) + \frac{\partial u}{\partial x} = -u\frac{1}{A}\frac{dA}{dx} \tag{2.2.1}$$

$$\frac{\partial u}{\partial t} + u\frac{\partial u}{\partial x} + \frac{1}{\rho}\frac{\partial p}{\partial x} = 0 \tag{2.2.2}$$

$$\frac{\partial s}{\partial t} + u\frac{\partial s}{\partial x} = 0 \tag{2.2.3}$$

One can easily recognize respectively the conservation Equation of mass, momentum and entropy.

$$\left(\frac{\partial}{\partial t} + u\frac{\partial}{\partial x}\right)\log\left[\frac{p^{1/\gamma}}{\rho}\exp\left(\frac{-s}{c_p}\right)\right] = 0 \tag{2.2.4}$$

In addition, assuming that the perturbations are small compared to the undisturbed steady flow ($\rho'/\rho \ll 1$), and expressing ρ, p, u and s as the following: $p = p\left(1+\frac{p'}{p}\right)$, $\rho = \rho\left(1+\frac{\rho'}{\rho}\right)$, $u = u\left(1+\frac{u'}{u}\right)$, $s = s\left(1+\frac{s'}{s}\right)$, one can linearise Equations 2.2.1, 2.2.2 and 2.2.3 to obtain:

$$\left(\frac{\partial}{\partial t} + u\frac{\partial}{\partial x}\right)\left(\frac{p'}{\gamma p}\right) + u\frac{\partial}{\partial x}\left(\frac{u'}{u}\right) = 0 \tag{2.2.5}$$

$$\left(\frac{\partial}{\partial t} + u\frac{\partial}{\partial x}\right)\left(\frac{u'}{u}\right) + \frac{c^2}{u}\frac{\partial}{\partial x}\left(\frac{p'}{\gamma p}\right) + \left(2\frac{u'}{u} - (\gamma-1)\frac{p'}{\gamma p}\right)\frac{du}{dx} = \frac{du}{dx}\frac{s'}{c_p} \tag{2.2.6}$$

$$\frac{s'}{c_p} = \frac{s'}{c_p}\left(t - \int^x \frac{d\xi}{du}\right) \tag{2.2.7}$$

Using Equations 2.2.4 and 2.2.7 gives:

$$\frac{p'}{\gamma p} - \frac{\rho'}{\rho} = \frac{s'}{c_p}\left(t - \int^x \frac{d\xi}{du}\right) \tag{2.2.8}$$

They defined the nozzle length as l with $0 \leqslant x \leqslant l$ and used the subscript 1 and 2 for respectively the inlet ($x < 0$) and the outlet flow ($x > l$). The pressure and velocity satisfy the general acoustic wave equations and are written as the following, where plus or minus stand respectively for a wave propagating in the same direction as the flow and in the opposite direction:

$$\frac{p'}{\gamma p} = P^+ exp\left[i\omega\left(t - \frac{x}{u+c}\right)\right] + P^- exp\left[i\omega\left(t - \frac{x}{u-c}\right)\right] \tag{2.2.9}$$

$$\frac{u'}{c} = U^+ exp\left[i\omega\left(t - \frac{x}{u+c}\right)\right] + U^- exp\left[i\omega\left(t - \frac{x}{u-c}\right)\right] \tag{2.2.10}$$

U and P are linked and $U^+ = P^+$ and $U^- = -P^-$, so that one can rewrite:

$$\frac{u'}{c} = P^+ exp\left[i\omega\left(t - \frac{x}{u+c}\right)\right] - P^- exp\left[i\omega\left(t - \frac{x}{u-c}\right)\right] \tag{2.2.11}$$

Also entropy can be expressed using ω, a radian frequency, convected at the velocity u:

$$\frac{s'}{c_p} = \sigma exp\left[i\omega\left(t - \frac{x}{u}\right)\right] \tag{2.2.12}$$

Marble & Candel [31] studied different type of flows but always with the compactness hypothesis. They studied for example the compact supercritical nozzle but also the compact subsonic nozzle and finally compact choked supercritical nozzle.

For the compact supercritical nozzle, they assume a quasi-steady flow and no heat losses, exchange or shock. Since the geometry is fixed, the fractional variation in density (Equation 2.2.13) is the same at the inlet and the outlet.

$$\frac{m'}{m} = \frac{1}{M}\left(\frac{u'}{u} + \frac{\rho'}{\rho}\right) \tag{2.2.13}$$

Assuming that the entropy is constant through the nozzle, the value 2.2.14 is the same at the inlet and the outlet.

$$\frac{s'}{c_p} \tag{2.2.14}$$

Using Equations 2.2.13 and 2.2.14, one can conclude that the stagnation temperature fluctuations is conserved and is expressed as the following:

$$\frac{T_t'}{T_t} = \frac{1}{1 + \frac{1}{2}(\gamma - 1)M^2}\left[\gamma\left(\frac{p'}{\gamma p}\right) - \frac{\rho'}{\rho} + (\gamma - 1)M\frac{u'}{c}\right] \tag{2.2.15}$$

$$where\ T_t \quad = \quad T(1 + \frac{(\gamma - 1)}{2}M^2)$$

The fractional mass flow variation can hence be deduced since it is directly proportional to the stagnation pressure and inversely proportional to the square root of stagnation temperature.

$$\frac{m'}{m} = \frac{1}{1 + \frac{1}{2}(\gamma - 1)M^2}\left[\frac{\gamma}{2}(1 - M^2)\frac{p'}{\gamma p} + \frac{\gamma + 1}{2}M\frac{u'}{c} + \frac{1}{2}(1 + \gamma M^2)\frac{\rho'}{\rho}\right] \tag{2.2.16}$$

Using Equations 2.2.16 and 2.2.13 give the equation below:

$$\frac{u'}{c} - \frac{\gamma}{2}M\left(\frac{p'}{\gamma p}\right) + \frac{1}{2}M\frac{\rho'}{\rho} = 0 \tag{2.2.17}$$

Finally using the above equation, $\frac{p'}{\gamma p}$ is constant at the inlet and the outlet, hence the entropy is also constant.

$$\frac{p'}{\gamma p} = \text{constant} \tag{2.2.18}$$

- For an acoustic wave, using $P_1^+ = U_1^+ = \varepsilon$ and $\sigma \equiv 0$ and Equation 2.2.17, one can evaluate $\frac{u'}{c_1}$ and $\frac{p'}{\gamma p_1}$ at $x = 0$ (the location of the discontinuity) from Equations 2.2.9 and 2.2.11, and finally obtain the reflected wave upstream:

$$P_1^- = \left[\frac{\left(1 - \frac{1}{2}(\gamma - 1)M_1\right)}{\left(1 + \frac{1}{2}(\gamma - 1)M_1\right)}\right]\varepsilon = \beta\ \varepsilon \tag{2.2.19}$$

As $M \longrightarrow 1$, $\beta \longrightarrow 1 - 2\left(\frac{\gamma - 1}{\gamma + 1}\right)$, using Equation 2.2.18: $\frac{p'}{\gamma p_1}(0_-, t) = \frac{p'}{\gamma p_2}(0_+, t)$

Then

$$\frac{p'}{\gamma p_2}(0_+,t) = \left[\frac{2}{\left(1+\frac{1}{2}(\gamma-1)M_1\right)}\right]\varepsilon\, e^{i\omega t} \tag{2.2.20}$$

Using Equation 2.2.17:

$$P_2^+ = \left[\frac{\left(1+\frac{1}{2}(\gamma-1)M_2\right)}{\left(1+\frac{1}{2}(\gamma-1)M_1\right)}\right]\varepsilon \tag{2.2.21}$$

$$P_2^- = \left[\frac{\left(1-\frac{1}{2}(\gamma-1)M_2\right)}{\left(1+\frac{1}{2}(\gamma-1)M_1\right)}\right]\varepsilon \tag{2.2.22}$$

- For a temperature disturbance, using P_1^+=0 but $\sigma \neq 0$ and Equation 2.2.17 gives:

$$P_1^- = \left[\frac{M_1}{\left(1+\frac{1}{2}(\gamma-1)M_1\right)}\right]\frac{\sigma}{2} \tag{2.2.23}$$

Using Equations 2.2.14, 2.2.17 and 2.2.18 gives:

$$P_2^+ = \left[\frac{\frac{1}{2}(M_2-M_1)}{\left(1+\frac{1}{2}(\gamma-1)M_1\right)}\right]\frac{\sigma}{2} \tag{2.2.24}$$

$$P_2^- = \left[-\frac{\frac{1}{2}(M_2+M_1)}{\left(1+\frac{1}{2}(\gamma-1)M_1\right)}\right]\frac{\sigma}{2} \tag{2.2.25}$$

For the compact subcritical nozzle:

- For a pressure perturbation, using P_1^+=U_1^+=ε, $\sigma \equiv 0$, Equations 2.2.13, 2.2.14 and 2.2.15 gives:

$$P_2^- = 0 \tag{2.2.26}$$

This means that there is no forward propagating wave and no upstream transmitted wave. Only P_1^- and P_2^+ remain and are defined as follows:

$$P_1^- = \left(\frac{M_2-M_1}{1-M_1}\right)\left(\frac{1+M_1}{M_2+M_1}\right)\left[\frac{1-\frac{1}{2}(\gamma-1)M_1M_2}{1+\frac{1}{2}(\gamma-1)M_1M_2}\right]\varepsilon \tag{2.2.27}$$

$$P_2^+ = \left(\frac{2}{1+M_2}\right)\left(\frac{1+M_1}{M_2+M_1}\right)\left[\frac{1+\frac{1}{2}(\gamma-1)M_2^2}{1+\frac{1}{2}(\gamma-1)M_1M_2}\right]\varepsilon \tag{2.2.28}$$

- For an entropic disturbance, using $P_1^+ = U_1^+ = P_2^- = 0$, $\sigma \neq 0$ and Equations 2.2.13, 2.2.14 and 2.2.15 gives:

$$P_1^- = -\left(\frac{M_2 - M_1}{1 - M_1}\right)\left[\frac{\frac{1}{2}M_1\sigma}{1 + \frac{1}{2}(\gamma - 1)M_1M_2}\right] \tag{2.2.29}$$

$$P_2^+ = \left(\frac{M_2 - M_1}{1 + M_2}\right)\left[\frac{\frac{1}{2}M_2\sigma}{1 + \frac{1}{2}(\gamma - 1)M_1M_2}\right] \tag{2.2.30}$$

For the compact shocked supercritical nozzle, the shock is located near the outlet with the velocity u_s' and subscript 3 stands for the state after the shock (see Figure 2.2.5).

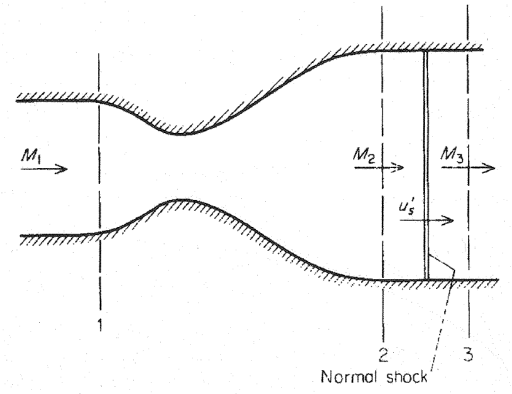

Figure 2.2.5: *Compact supersonic nozzle with normal shock downstream with subscripts.*

Using $P_1^+ = U_1^+ = 0$, $\sigma \neq 0$ and Equations 2.2.23, 2.2.24 and 2.2.25, the normalized travelling pressure are:

$$\frac{P_1^-}{\sigma} = -\frac{\frac{1}{2}M_1}{1 + \frac{1}{2}(\gamma - 1)M_1} \tag{2.2.31}$$

$$\frac{P_3^+}{\sigma} = \left(\frac{-(1 + M_2^2)M_1 + 2M_2^2M_3^2}{1 + M_2^2 + 2M_2^2M_3^2}\right)\left[\frac{\frac{1}{2}}{1 + \frac{1}{2}(\gamma - 1)M_1}\right] \tag{2.2.32}$$

For this case, P_1^- is equal to P_1^- obtained for the supercritical shocked nozzle since the presence of the shock located downstream of the nozzle cannot affect the characteristics upstream.

With computing power improvement, Candel & Marble [31] research have been completed by Bake *et* al. [2] and [4] for subsonic nozzle flows and also by Leyko *et* al. [29] for the supersonic nozzle with shock. The relevant result obtained by Leyko *et* al. [29] is that entropy fluctuations can be created through the interaction of a shock and an acoustic wave, then reflections at the exit of the channel have strong effect on the measured acoustical signal. Bake [2] compared Marble & Candel [31] theoretical results with his results using a nozzle and a diffuser. According to Bake *et* al. [2] large differences are observed and the possible reason which is mentioned is the compactness criterion of the nozzle.

The solutions obtained by Marble & Candel [31] are valid for a compact nozzle and if the excitation amplitudes are small. That is why, the last part of their paper deals with a **supercritical nozzle**

of finite length. The main idea of the last part is that the fluctuation magnitude and the reduced frequency are strongly connected. In addition, amplitude are even higher as the term $M_1 - M_2$ is large but also as the reduced frequency rises; a possible interaction between P^+ and P^- waves can increase the disturbance magnitude.

In order to complete Marble & Candel [31] work, the work of Bohn [9] must be presented. Bohn worked on a finite length subsonic nozzle. In the same way as Marble & Candel [31] and by using the same assumptions, Bohn give a general approach for solving the linearised equations in the high frequency limit. The response is decomposed in terms of transmitted and reflected acoustic waves. A solution for high frequency disturbances is used in order to normalize the calculations. This normalisation allows to conclude that the transmitted waves created by two acoustic disturbances can be expressed as a single function of frequency for a given M_1 and M_2. Later Moase *et* al. [33] propose an analytical model taking into account arbitrary shapes. Moase [33] give a set of boundary conditions to complete existing work about nozzle with random geometry. Giauque & Huet [20] revisit Moase model [33] and apply it to subcritical nozzles with complex geometry, the issue of the nozzle compactness being also addressed. In addition, one important conclusion of their study is that in the subcritical range, the indirect combustion noise is not the only major responsible for the acoustic disturbance for the configuration of Bake *et* al..

Numerical approach

Numerical simulations are used in order to validate the aforementioned analysis and to analyse the validity of assumptions used are preformed.

Bloy [8] was the first to compute the indirect combustion noise. He uses the method of characteristics in an unsteady one-dimensional subsonic flow through a nozzle produced by the convection of a temperature disturbance. In addition, upstream and downstream pressure waves are generated in agreement with experimental observations.

Mühlbauer *et* al. [34] use the U-RANS (Unsteady Reynolds Average Navier Stokes) technique with a $k - \varepsilon$ turbulent model to simulate the acoustic disturbance observed in the EWG test facility. Entropy waves are generated electrically and accelerated through a convergent-divergent nozzle. The results show a good agreement with the experimental data.

Another available numerical tool is LES (Large Eddy Simulation), Leyko *et* al. [29] use the AVBP code from CERFACS to compare data from the EWG test ring with their simulation see Figure 2.2.6. It appears that using a 3-D model instead of a 2-D asymmetrical does not significantly affect the pressure signal.

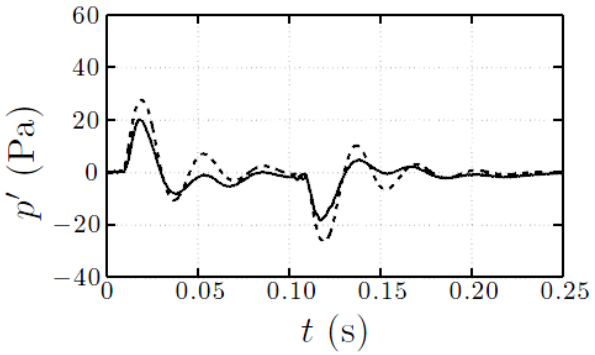

Figure 2.2.6: *Fluctuating pressure downstream of the nozzle over time, the pressure sensor is located at 1150mm downstream of the nozzle: (−) measured pressure, (−−) simulated pressure; from Leyko et al. [29].*

Richter *et* al. [41] use an Hybrid or Zonal approach to solve the noise of an entropic source. Two steps are needed, first accelerated entropy perturbations have to be obtained numerically using 2-D U-RANS. Then, data are injected in a CAA code using Neumann or Dirichlet boundary conditions. The propagation of the acoustic waves is solved using Euler equations (linearised or not). Even though, the acoustic formulations obtained from linearised or non-linearised are quite similar, substantial pressure signal differences are observed.

2.2.2 Noise generated through turbine stages

Currently, several models exist for the modelling of downstream noise after one or more turbine stages.

Analytical Approach

Cumpsty & Marble [16] simplify a one turbine stage using two main hypothesis. First, the flow through a stage is considered as steady (upstream and downstream solutions are obtained from the continuity equations). Secondly, the flow is treated as two-dimensional in the axial-tangential plan. Dispersion equations are obtained from the conservation equations (mass flow or corrected mass flow if a shock occurs, entropy, enthalpy and outlet Mach number). Hence, they solve it numerically by using a matrix form. The relevant result of their work is that from two identical stages, the acoustic power is larger than a single stage. Increasing the number of stages modifies the spectrum but does not influence the acoustic power. Their predictions agree fairly well with measurements on real a engine.

Kaji & Okazaki [23] use a blade row model or the semi-actuator disk theory to find the transfer functions. The idea is to assume the blade chord to be negligible. They also solve the problem using a potential technique [24] (when the blade chord is taken into account). They conclude that the difference is not significant and that the semi-actuator disk theory performs well for a one stage turbine. One can criticize this assumption since geometry and radial modes are not taken into account in this resolution.

The works of Muir is an extension of Kaji & Okazaki [23] but in three-dimensions. Muir first uses it on a single blade row [35] and later on a multiple blade rows [36]. The average frequency approach is used in order to remove the dependency between the model and the wavelength of the incident sound field. According to Muir, the Kaji & Okazaki model has two main restrictions or limits. No radial mode can be taken into account due to the 2-D geometry and the fact that the flow must be subsonic. Muir's model can (to first order) discard those two limitations and in addition take into account the blade twist (the leading edge and trailing edge angles) which has an important effect on the wave reflection after one turbine stage. The conclusion is that the blade twist has a non negligible effect on the wave reflection coefficient through a turbine stage.

Pickett [38] analytically determines the pressure level generated through a turbine stage by the convection of a temperature wave. He solves the total noise generated by assuming each stage contribution to be independent and adds each terms. This hypothesis is not correct as Cumpsty & Marble [15] show that in particular configurations the coupling between different stages could be important.

Numerical Approach

Leyko *et* al. [28] perform unsteady aerodynamic simulation of a combustion chamber followed by a stator. They compare their results with Cumpsty & Marble [16] predictions. They use a compressible 3-D LES method with the AVBP code from CERFACS to compute the upstream perturbations (acoustic, entropic or vorticity) before the stator. In their configuration, only acoustic and entropic waves produce noise and no acoustic wave are generated by vorticity because they assume a purely axial flow. Their results are in good agreement with the analytical results from Cumpsty & Marble

[16]. In Figure 2.2.7 on the left hand side, one can see that the upstream acoustic wave calculated using 2-D LES simulation is fairly similar to the analytical approach given by Cumpsty & Marble [16], meaning that the stator is acoustically compact. In Figure 2.2.7 on the right hand side, for an upstream entropic wave the simulation matches quite well the Cumpsty & Marble [16] model but only for low frequencies. This means that in this case, the dimension of the blade has to be taken into account when calculating the transfer functions.

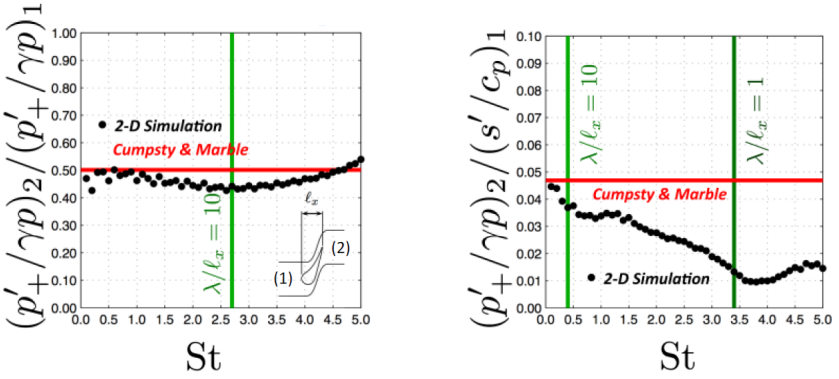

(a) *Upstream acoustic wave* $(\frac{p'_+}{\gamma p})_1$ (b) *Upstream entropic wave* $(\frac{s'}{c_p})_1$

Figure 2.2.7: *Transfer functions from Leyko et al [28].*

The same conclusion is established by Leyko *et* al. when computing the acoustic and the entropic powers. For an acoustic upstream wave, the differences between their 2-D simulation and Cumpsty & Marble [16] are negligible. On the other hand the differences are significant for an entropic upstream wave, especially for high frequencies. The 2-D Cumpsty & Marble [16] model appears to over-estimate the entropic power see Figure 2.2.8. The authors conclude that Cumpsty & Marble [16] seems to be a very good first order model for combustion noise at low frequencies.

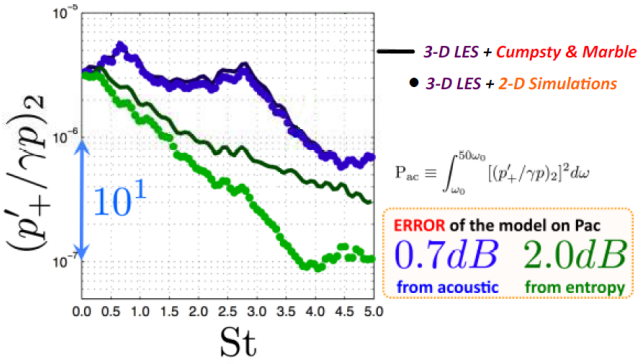

Figure 2.2.8: *From acoustic: blue − and ∘; from entropy: green − and ∘.*

2.3 Conclusion

The combustion noise has two origins. It can be created by the unsteady heat release fluctuation in the combustion chamber and then be called Direct combustion noise. It can also be related to the acceleration in a nozzle or a turbine row of temperature or vorticity inhomogeneities created by the flame and be called Indirect combustion noise.

The direct combustion noise is a complex problem and no general analytical solution has been found to accurately describe heat release and noise radiation. In addition, more experimental facilities

would help solve the problem faster. Finally, numerical tools exist and LES or DNS can give valuable insight into this problem.

After a combustion chamber, two devices are likely to produce indirect combustion noise: the nozzle and the turbine. Experimentally, only the flow passing through a nozzle has been studied so far. Analytically, both devices have been solved by Marble & Candel [31] and others. Numerically, several approaches have been used for the nozzle; but for the turbine; only few LES 2-D simulation on an one stage turbine has been carried.

3 Discern project

3.1 What is Discern?

DISCERN stands for Direct and Indirect Sound Sources in Combustion: Evaluation and Reduction of Noise. It is an Industrial research which aims at characterizing the direct and indirect combustion noise sources involved in sound emission in industrial processes mainly on aero- and power gas turbines. Direct as well as indirect noises must be studied in more details to precisely **discern** their respective contribution to combustion noise. The project involves three partners with a wide range of complementary skills on the different approaches (EMC2, CERFACS and ONERA) see Figure 3.1.1. The EM2C Laboratory is a CNRS research unit located at Ecole Centrale Paris. CERFACS is the Centre Européen de Recherche et de Formation Avancées en Calcul Scientifique and is a research organization developing advanced methods for the numerical simulation and the algorithmic solution of large scientific and technological problems of interest. The four principal objectives of this project are [18]:

1 To provide experimental databases of a practical configuration featuring both types of noise sources in a well-controlled acoustic environment. To experiment and validate diagnostics and post-processing methods for the determination of the different noise contributions using results obtained in 2.

2 To provide HFLES databases of the same configuration. To conduct exhaustive comparisons with the experimental databases obtained in 1. in order to mutually validate both strategies. To propose adapted post-processing methods for the determination of the different noise contributions.

3 To investigate and model the influence of the exhaust design on the indirect noise contribution based on the experimental and numerical fields made available in 1. and 2., and on dedicated LES. To propose modifications of the nozzle design to test noise reduction efficiency.

4 To help in the development of practical predictive low-order methods for the discrimination of direct and indirect noise sources, including the models elaborated in 3. To validate these tools on the databases developed in 1. and 2.

This internship is a part of this project and is strongly linked with the Task 3. which will be developed more precisely in the next section.

3.2 Purpose of the Internship linked with Task 3

According to Bloy [8], it is expected that the exhaust geometry, through modifications of the velocity profile in the nozzle, has a significant impact on the indirect noise generation and propagation. No clear demonstration of this has been carried out up to now. That is why ONERA LES solver CEDRE will be used to compute acoustic propagation and indirect noise generation downstream the chamber on several different shape of nozzle. This approach will allow to investigate for the first time the influence of the nozzle geometry on noise production and propagation in 3-D. The main objective of this task is the investigation and the modelling of the exhaust geometry influence on the noise propagation and generation. A low order model will be developed that will rely on averaged fields of the relevant quantities (such as pressure, temperature and velocity). This task can be divided in three sub-task which are [18]:

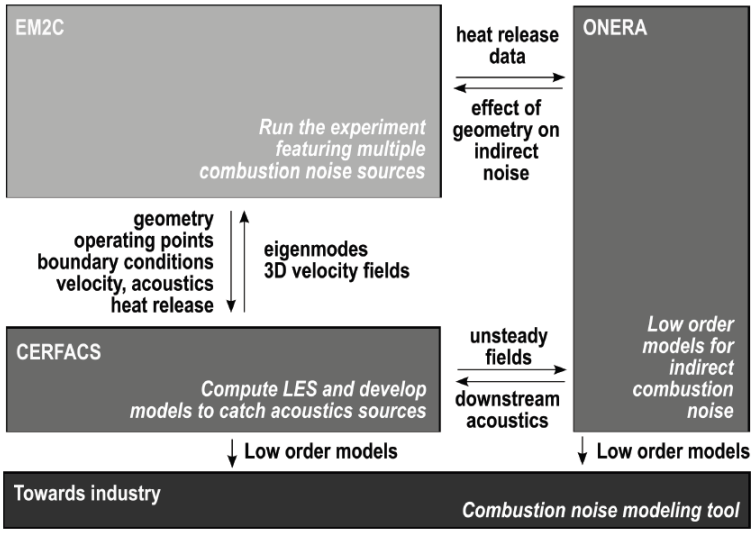

Figure 3.1.1: *Diagram of the project organization [18].*

4.1 Improvement of numerical methods: A proper injection of fluctuating quantities following prescribed temporal and/or spectral contents is a mandatory step to this task. A characteristics based boundary condition able to deal with such complex requirements will be implemented and validated in ONERA LES solver CEDRE.

4.2 Detailed LES simulations of the exhaust region: Several geometries, defined together with the partners will be computed, making use of the data provided by EM2C and CERFACS. Using the results obtained in this task, correlations between indirect combustion noise levels and averaged flow fields will be studied.

4.3 Development of a low order model for indirect combustion noise generation: Using the results from Sub-Task 4.2, as well as the expertise of the partners, ONERA will develop a low order model for the indirect combustion noise. The model will include the influence of the relevant design parameters of the exhaust nozzle and provide correlations between acoustic levels, geometrical parameters and incoming entropy fluctuations in the nozzle.

This internship will hence be focused mainly on the sub-task 4.1 and the pursue of the project will be performed during a PhD at ONERA.

4 Presentation of the Numerical tools

4.1 GAMBIT

The historical editor of GAMBIT was Fluent Inc, it is now owned by ANSYS, Inc. GAMBIT is a preprocessor for engineering analysis. It has an easy-to-use and a comprehensive interface which allows the rapid creation of the geometry and/or the mesh. The surface and the wire-frame features are powerful and simple even for detailed models. In addition, a geometric clean-up tools can be used to quickly identify certain geometrical entities that might cause quality problems during surface meshing.

4.2 CENTAUR

CENTAUR is a software developed by CentaurSoft. It is a really good unstructured mesher with advanced features to:
- Define different characteristic element length for different part of the geometry.
- Setting grid parameters such as stretching factor for the characteristic mesh element length.
- Create an adaptive mesh.
- Create groups and specifying boundary conditions.
- User-Controlled Mesh Clustering (Sources).
- View the generated grids.
- Repair and clean the geometry.

The CENTAUR grid generator produces high quality grids with minimal user interaction for a wide range of engineering problems (fluids mechanics, aerodynamics, solids mechanics, heat transfer and combustion). CENTAUR can also generate structured mesh but also combines structured and unstructured grids via a hybrid (prismatic/hexahedral/pyramidal/tetrahedral) meshing strategy. It is powerful at meshing different parts of 2-D or 3-D geometries with different mesh elements. In our case, the mesh will be fully tetrahedral.

4.3 CEDRE

The Navier-Stokes solver, CHARME, is one of the numerous solver of the CEDRE code. CEDRE code is a fully unstructured solver developed at ONERA with main applications in the energetics and propulsion fields. It can be coupled with other solvers to perform multi-physics simulations [13] and [37]. It is based on a cell centred finite volume approach that deals with generalized polyhedral grids (the cells can have any number of faces and faces any number of vertices). Spatial discretization is based on second order MUSCL schemes, which MUSCL stands for Monotone Upstream-centered Schemes for Conservation Laws proposed by van Leer [27]. The time integration is based on explicit or implicit GMRES schemes (up to third order); GMRES stands for Generalized Minimal Residual Methods described by Saad *et* al. [43]. Recent developments on the MUSCL schemes were integrated in the latest version of the used CEDRE code. In our study, the temporal scheme used for the numerical simulation is a Runge-Kutta explicit method with 3 approximations (RK3). In addition, several turbulence models are available ranking from one-equation or two equations, RANS (Reynolds-Averaged Navier-Stokes equations) models to Large Eddy Simulation Smagorinsky models (used in this study) and DES (Detached Eddy Simulation).

5 Numerical simulations

5.1 Modelling the geometry with GAMBIT

The geometry of the system is based on the CAD file given by the EM2C Laboratory. This file was used to build the test bench located at EM2C Laboratory. One can see in Figure 5.1.1, the different parts of the setup on the left hand side figure from left to right the injector, the combustion chamber and the nozzle respectively. But as mentioned in the precedent section, the numerical simulation will be performed downstream of the combustion chamber. The final geometry is shown in Figure 5.1.2. This geometry is created using GAMBIT and is composed of three surfaces, the Inlet, the Outlet and the Wall. Upstream of the nozzle, the length of the combustion chamber was reduced and only 4.28 cm is kept. It seems reasonable that at 3/4 of the combustion chamber the flame is not present in this area and thus that combustion has already occurred. In addition, a cylindrical part (15 cm) is added after the nozzle to "see" the behaviour of the fluid at the end of the nozzle and to control turbulent structures effects. The total length of the geometry is 54.125 cm.

Note that even if the Inlet has a squared shape and the Outlet a circular shape, the cross-sectional area is the same (49 cm^2). In the subsonic case, the inlet and the outlet speed flow is hence the same.

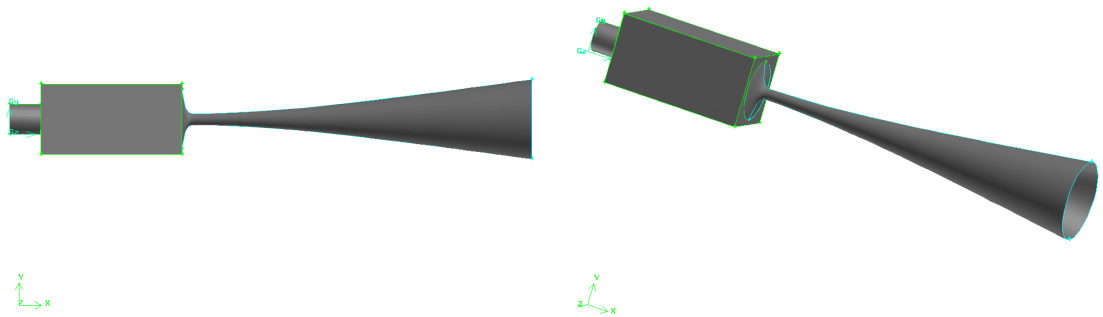

Figure 5.1.1: *Geometry of the test bench at the EM2C.*

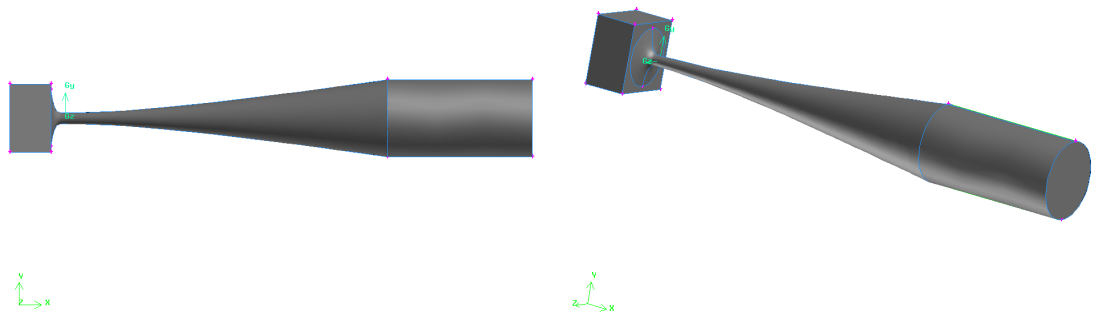

Figure 5.1.2: *Geometry used for the numerical simulation.*

5.2 Meshing using the CENTAUR grid generator

Once the geometry has been generated, the CENTAUR grid generator is used to create the meshes. It is possible to mesh the geometry using GAMBIT but as described in Section 4.2, more features are available in CENTAUR. In order to generate the mesh correctly, some calculations have to be done before. The minimum number of points per wavelengths needed for the code CEDRE to obtain an reasonable dissipation is 20 points per wavelengths. All the following calculations will hence be performed with that number of points.

The size of the elements used for the mesh generation is found by doing some calculations regarding the length of the geometry, the minimum and the maximum frequency. The used values for generating the CAD file and then the bench test are given below in Table 5.2.1:

Inlet	$T = 1300$ K $M = 0.01081$ or $u = 7.59$ m/s with $c = \sqrt{1300 \times R \times \gamma} = 702$ m/s
Outlet	$P = 202600$ Pa
All domain	$\gamma = 1.32$ $R = 287$ J/kg.K

Table 5.2.1: Data used for the geometry generation.

If u is the fluid velocity along the axial x-coordinate of the nozzle, c the fluid mean sound speed and f the frequency of the acoustic waves, one can write the following relation for the forward propagating wave:

$\lambda = \frac{u+c}{f}$. λ increases when f decreases. The frequency bandwidth used in this study is $80 \leq f \leq 600$ Hz.

Acoustically, the smallest frequency will give the minimum simulation time, for example after four periods the simulation time should be $\frac{1}{80} \times 4 = 0.05$ms.

The smallest elements size is related to the maximum frequency such that:

$$\lambda_{acoumin} = \frac{7.59 + 702}{fmax} = \frac{7.59 + 702}{600} = 1.1827 \text{ m } \lambda_{entropic} = \frac{u}{f_{max}} = \frac{7.59}{600} = 0.01265 \text{ m}$$

For 20 points per wavelengths it leads to:

$$\Delta x_{acou} = \frac{u + c}{20 \times fmax} = \frac{\lambda_{acou}}{20} = 0.05913 \text{ m}$$

$$\Delta x_{entro} = \frac{u}{20 \times fmax} = \frac{7.59}{20 \times 600} = 6.325 \times 10^{-4} \text{ m}$$

One can observe that the entropy wave is the one imposing the most stringent condition on the element size.

In order to obtain around 32 millions elements for the fine mesh, a smaller element size than Δx_{entro} of length 0.54 mm is used. This corresponds to approximately 23 points per wavelengths. Close to the outlet (35 cm after the throat), a stretching factor is applied in order to avoid numerical reflection effects but also to dissipate most of the unsteady vorticity fluctuations. The element length increase is such that $\Delta x_{n+1} = 1.03 x_n$. A 5 million tetrahedral elements coarse mesh is also created with a mesh size of 2 mm. The two meshes are showed in Figure 5.2.1. In addition, Figures 5.2.2 and 5.2.3 give an overall view of the mesh and also illustrate the stretching factor used. This can be seen when comparing the number of faces at the Inlet with the number of faces at the Outlet.

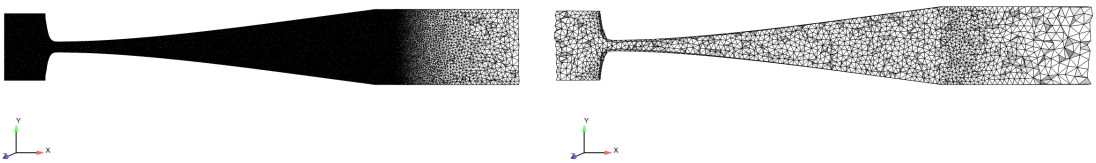

Figure 5.2.1: *Fine Mesh and Corse Mesh.*

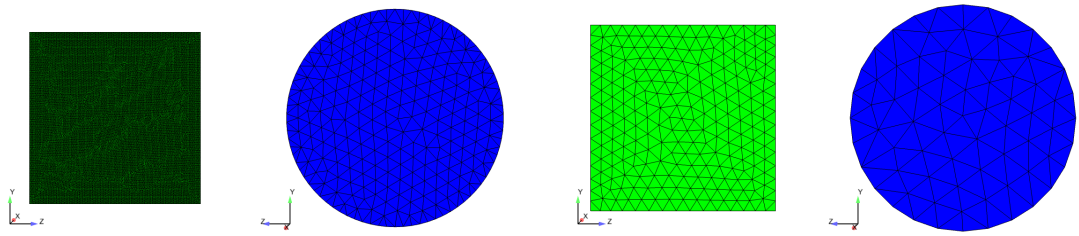

Figure 5.2.2: *Fine Mesh (left) and Coarse Mesh (right) of the Inlet (green) and the Outlet(blue).*

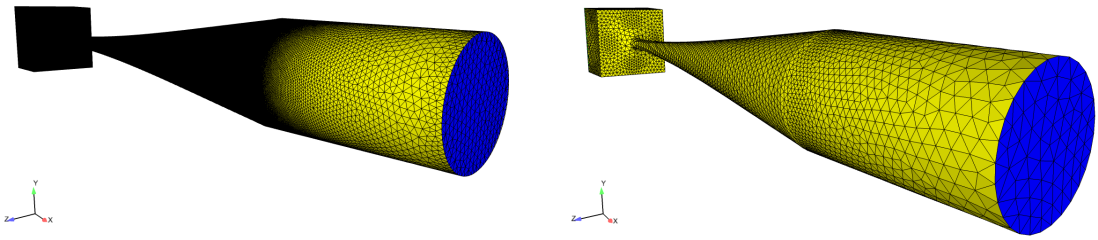

Figure 5.2.3: *Sideview of the Fine Mesh (left) and the Coarse Mesh (right).*

5.3 Simulation settings

The computational setup is presented in this section. First, the meshes are split into several smaller pieces of mesh during the calculation process. For the fine mesh, 480 pieces were created and 480 processors were used for each calculations. For the coarse mesh, 128 processors were used during the calculation.

5.3.1 The turbulent model

The flow modelling approach used in this study is the Large Eddy Simulation (LES). The LES approach can be interpreted as a low-pass filtering method. This filtering method is applied to the Navier-Stokes equations to eliminate small scales of the solution and therefore solve the structures greater than the mesh size. The eddy viscosity model used is the Smagorinsky's model. This model is based upon four hypothesis:

- The filtered structures are locally proportional to the mesh size.
- Those structures effects on larger scales are isotrop and can be seen as a turbulent viscosity.

- Energy production and dissipation of the small scales are in equilibrium, meaning that smaller scales than the cut-off length scale and the cut-off time scale are eliminated.
- Negligible compressibility effect.

The CEDRE code preprocessing software used to implement all the conditions is called EPICEA. The default settings proposed by EPICEA for the different turbulent quantities are used.

5.3.2 The wall model

The code CEDRE allows the user to access two different conventional wall laws. They are both based on the local equilibrium assumption, i.e. they mimic the behavior of a zero pressure gradient boundary layer following the log-law. Conventional wall laws quickly reach their limits when flows develop boundary layers with non-zero pressure gradients. The wall law used base is called the Simple Integrated Boundary Layer Equations (SIBLE) developed by F. Chedevergne [12].

A system composed of simple 1-D boundary layer equations is solved efficiently by recurrence for each cells on the wall. The two controlling features are defined respectively as the number of points N in a geometrical series with a constant ratio r. The mixing length model adopted in the SIBLE wall model eliminates the limitation of conventional wall laws while ensuring a high level of precision in both attached and separated flows. It can compute complex aerothermodynamic configurations on coarse grids with a satisfactory precision. In our case, N is set at 20 and the constant ratio r at 1.1.

5.3.3 Temporal scheme

The temporal scheme used for the numerical simulation is a Runge-Kutta explicit method with 3 approximations (RK3). It is an explicit time marching scheme. For stability and numerical convergence of the calculation, the Courant-Friedrichs-Lewy condition (CFL condition) should be satisfied. The CFL condition gives a time step, the time step used for numerical calculation must be less than the time given by the CFL condition. Otherwise the simulation will produce incorrect results as the information will never be propagated form one cell to its neighbouring cells. In the one dimensional case, the CFL acoustic maximum is defined as:

$$CFL_{acou} = \frac{\Delta t(c+u)}{\Delta x} \leq C_{max}$$

where Δt is the time step, Δx the interval length and $u + c$ is the acoustic wave velocity. For an explicit scheme, in code CEDRE the typical used value for $C_{max} = 0.5$. Using the data given in Table 5.2.1, the theoretical Δt should be for the fine mesh:

$$CFL_{acou} = \frac{\Delta t(c+u)}{\Delta x} = 0.5 \tag{5.3.1}$$

$$\Rightarrow \Delta t = \frac{\Delta x}{(c+u)} = \frac{0.5 \times 5.4 \times 10^{-4}}{1.8 \times 702} \approx 2.14 \times 10^{-7}\text{s} \tag{5.3.2}$$

The CFL condition is a necessary condition but may be not sufficient for the convergence of the calculation. Since this stability criterion gave problem during this study a smaller time step has been used for stability. In the study, the time step for the fine mesh is $\Delta t = 3 \times 10^{-8}$ s and for the coarse mesh $\Delta t = 5 \times 10^{-8}$ s which corresponds to a CFL of 0.07 and 0.117 respectively.

5.3.4 The initial conditions file

A solution from a one dimensional isentropic perfect gas flow in a variable section duct is used as an initial solution to reduce the transient time. It is based on the conditions provided by the test bench

which are given in Table 5.2.1. The computation of the field and the equations solved are described in the Appendix B. The general field of the flow can be seen in Figure 5.3.1. First, a one dimensional field over the x-direction is calculated, this field is then spatially spread in the y- and z-directions.

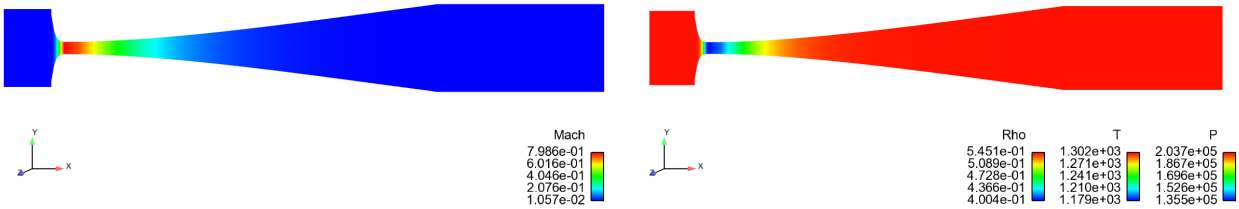

Figure 5.3.1: *Meanflow fields used as an initial solution.*

5.3.5 Non reflective Boundary condition

Non reflective boundary condition is used at the Inlet and the Outlet surfaces. This boundary condition was recently integrated in code CEDRE. It is based on the 3-D NSCBC (Navier-Stokes Characteristic Boundary Conditions) approach described by Lodato *et* al. [30]. At the Inlet, the temperature and the velocity and passive scalar are imposed. A global relaxation parameter called σ_{in} is used. This parameter controls the reflectiveness of the boundary and acts as the stiffness of a spring. A large value will make the system more reflective as the velocity and/or the temperature cannot deflect from the chosen values. On the other side, if σ_{in} is small, the system is less-reflective but then temperature and/or velocity can drift more easily. At the Outlet, the pressure is imposed. Here also a relaxation term σ_{out} is added to control acoustic reflection. This term has the same behaviour as σ_{in} and the value must be chosen carefully. In our study, σ_{in} and σ_{out} are chosen as 0.5 and 1 respectively. In addition, from the previous Subsection 5.3.4, at the Outlet the pressure is imposed to be 202600 Pa and at the Inlet the axial velocity on the x-direction and the temperature are fixed as 7.6456 m/s and 1300 K respectively.

5.3.6 Sensors integration

In order to control and follow which phenomena occur in the nozzle, it is necessary to have sensors. A sensor captures the pressure, temperature, velocities and density, it is cheap and the storage place is small. A total of 1368 sensors are placed strategically inside the domain. For example, 41 sensors are placed radially and define a "plane of sensor" see Figure 5.3.2. In total 32 planes and 56 single sensors placed on the axial direction of the nozzle are used. All single sensors are located on the x-axis. In Figure 5.3.3, one can see from left to right:

- 13 planes in the combustion chamber spaced every 0.00375m.
- 4 single sensor spaced by 0.00125m.
- 7 planes are used close to the throat, those planes are spaced every 0.00125m.
- 52 single sensors spaced every 0.00625m are used to capture behaviour of the field in the divergent part.
- 12 planes of sensors after the divergent part, the space between the planes is 0.0125m.

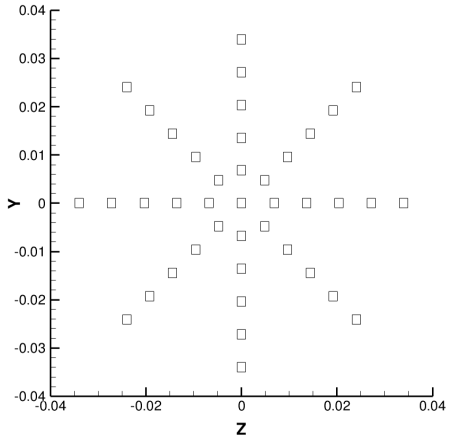

Figure 5.3.2: *A plane of sensors.*

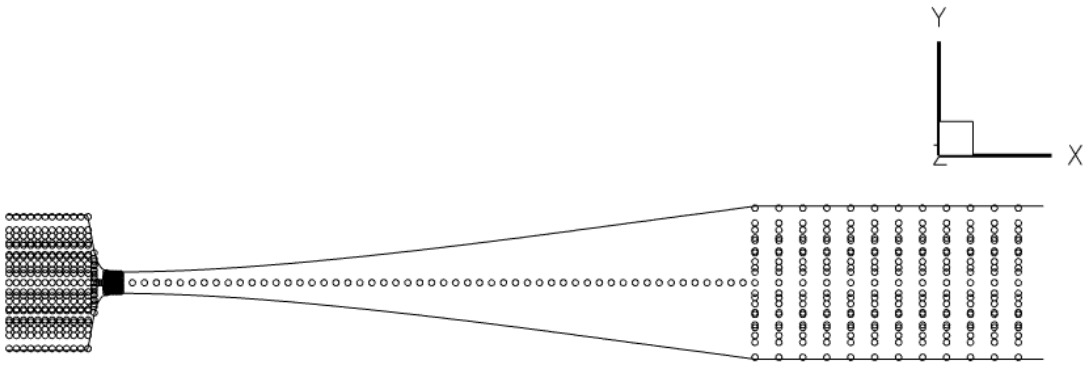

Figure 5.3.3: *View of the sensors along the nozzle direction.*

6 Initialisation and stability problems

The settings have been prepared and explained in the Section 5, the initialisation and some stability problems will now be presented below.

6.1 Mach stabilisation problem at the throat

As mentioned before the relaxation parameter σ_{in} is fixed at 0.5 in order to keep a less reflecting boundary. This allows the velocity to slip from its target value and fluctuate over time. This is critical for the Mach number at the throat which is strongly linked with the injected mass flow. Figure 6.1.1 shows the different positions of the sections. On the left hand side of Figure 6.1.2, one can see the Mach number variation over time at four different positions close to the throat. The distance between the two consecutive sections is 0.00125m. The section denoted as $Section_{17}$ is the theoretical position of the throat, the Mach number at this position varies from 0.81 to 0.86. The maximum Mach number is located at $Section_{20}$ (3.75mm) after the theoretical position of the throat. This feature can be explained by the creation of a boundary layer along the wall close to the nozzle, the layer reducing the cross-sectional area and then translating the theoretical nozzle position. Note that the maximum Mach number varies between 0.87 and 0.97 which is much higher than the expected 0.8 value. On the right hand side of Figure 6.1.2, the velocity fluctuations (V_x) at different sections are shown. In

Figure 6.1.3, the velocity fluctuations at $Section_{17}$ and at $Section_1$ (close to the Inlet) are plotted. The two curves have the same trend and differ only in their amplitude which is more or less doubled.

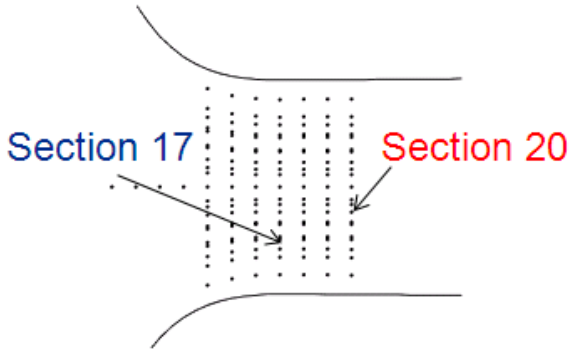

Figure 6.1.1: *Position of the sections close to the throat.*

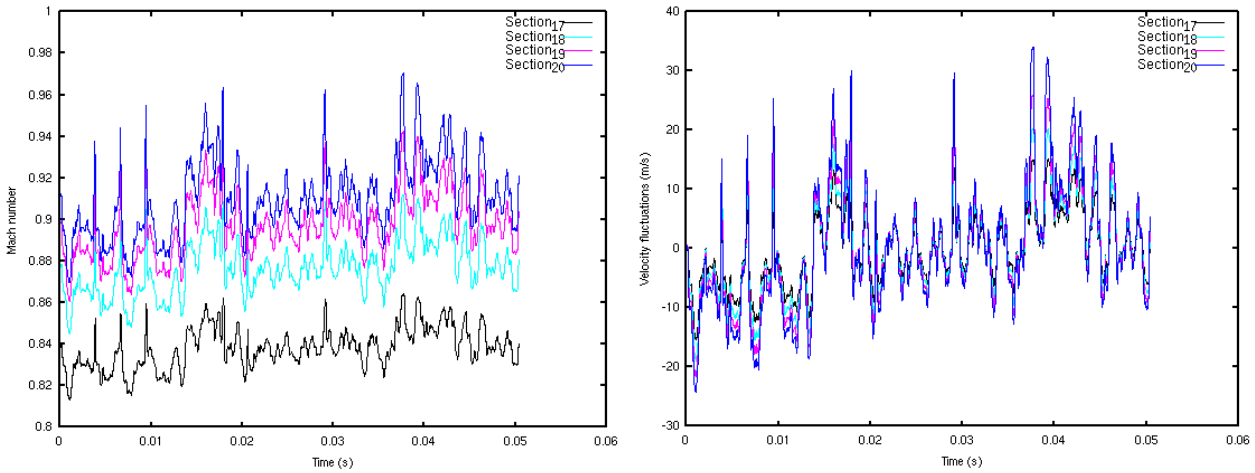

Figure 6.1.2: *Left hand side: Mach number at four different sections close to the throat. Right hand side: V_x velocity fluctuations at four different sections close to the throat. For both: $Section_{17}$ (black), $Section_{18}$ (cyan), $Section_{19}$ (magenta), $Section_{20}$ (blue).*

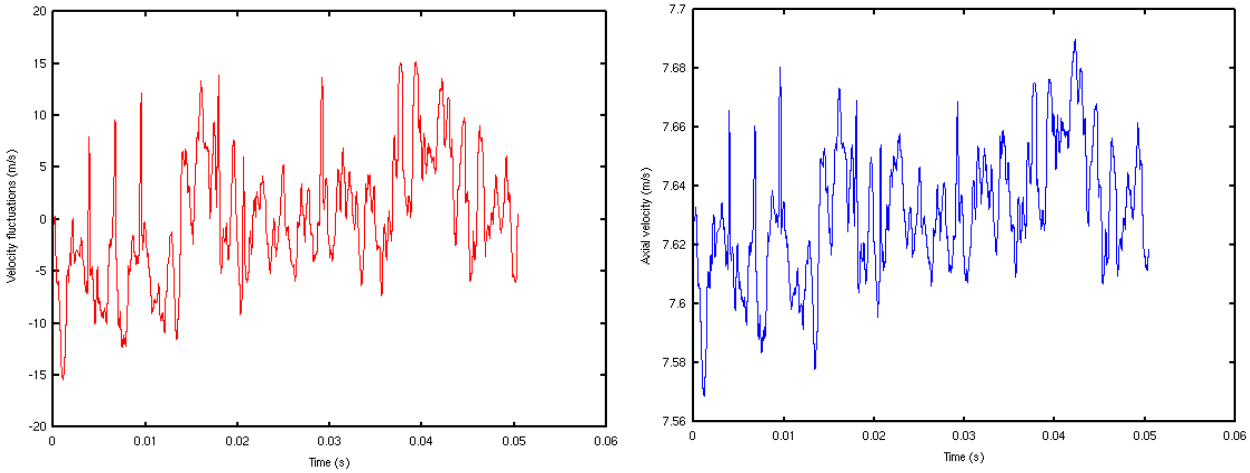

Figure 6.1.3: *Left hand side: Velocity fluctuations at* $Section_{17}$*. Right hand side: Axial velocity at* $Section_1$ *close to the Inlet.*

6.2 Boundary conditions stability issues

An unexpected feature occurred during the numerical simulation, it appears that the flow detaches from the wall inside the divergent leading to the development of strong turbulent structures and the creation of a jet. This phenomenon can be seen in Figure 6.2.1. The recirculation zones are also visible and the flow detached around 6.8 cm after the nozzle. This creates a jet in the divergent part. The vorticity is strongly increased and several turbulent structures flow through the Outlet. In order to see these structures, the vorticity and the Q-criterion defined by Hunt *et* al. [22] are calculated. They are defined as the following:

$$\overrightarrow{Rot}\overrightarrow{V} = \nabla \times \overrightarrow{V} \tag{6.2.1}$$

and

$$Q = \frac{1}{2}(\Omega_{ij}\Omega_{ij} - S_{ij}S_{ij}) \tag{6.2.2}$$

$$\Omega_{ij} = \frac{1}{2}(u_{ij} - u_{ji}) \tag{6.2.3}$$

$$S_{ij} = \frac{1}{2}(u_{ij} + u_{ji}) \tag{6.2.4}$$

Q is the second invariant of ∇u, it locates the regions where rotation dominates strain in the flow. Ω_{ij} and S_{ij} denote the antisymmetric and symmetric parts of ∇u. When $Q > 0$ means that rotation dominates deformation or that a vortex is coherent. The absolute value of the vorticity and the Q-criterion are shown in Figure 6.2.2. One can see the advantages of the Q-criterion compared to the vorticity which can represent only the vortex region.

In addition, the present implementation of non-reflecting boundary conditions generates over time some high frequency instabilities. In Figure 6.2.3, one can see "check pattern" instabilities on the pressure, the temperature. This happens also for the velocity, see Figure 6.2.4, where two views of the axial velocity is shown, inside the domain the velocity is around 45 m/s but at the Outlet face it is -39 m/s. Generally a non physical solution appears in a cell and spreads to its neighbours.

Those instabilities lead to a crash due to thermodynamical properties limits ($T > 4000$ K or T becomes negative) at the Outlet. As the non-reflecting boundary conditions is quite recent the debuging of this problem is in progress. The bug origin might be related to the 3-D NSCBC boundary condition and CEDRE spatial scheme coupling but this has to be confirmed.

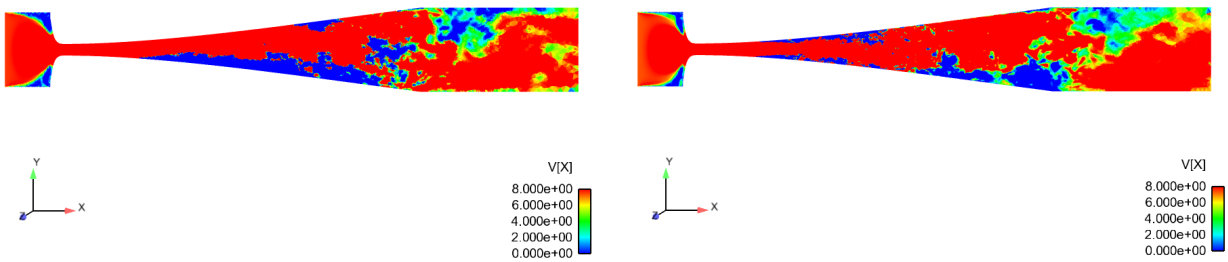

Figure 6.2.1: *Longitudinal cut coloured by axial velocity: Coarse mesh (left), Fine mesh (right).*

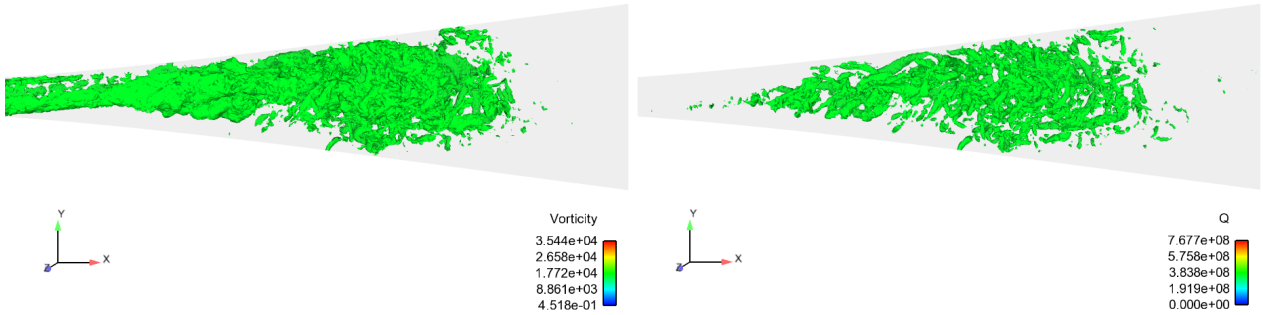

Figure 6.2.2: *Isosurfaces of the absolute vorticity (left) and isosurface of the Q-criterion (right).*

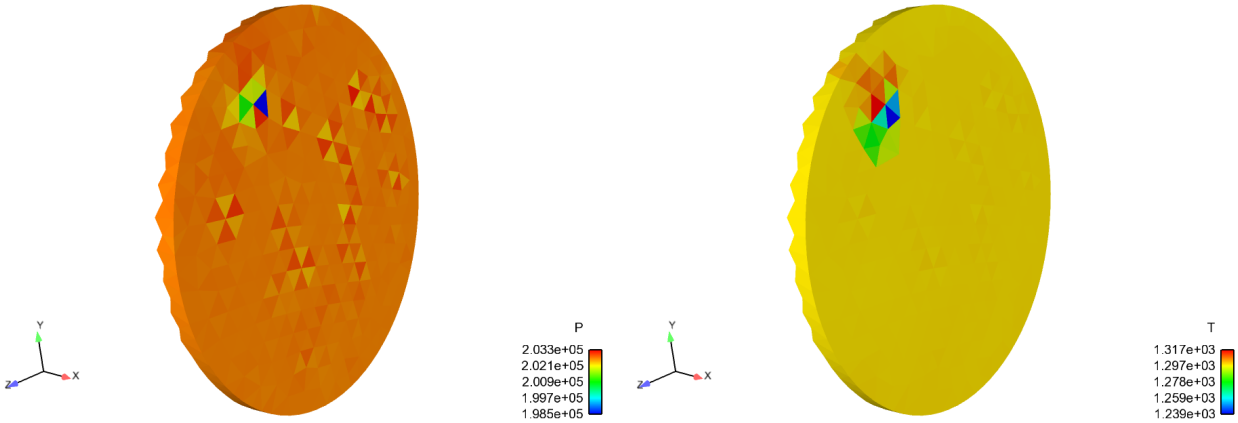

Figure 6.2.3: *Outlet view colored by the pressure (left) and by the temperature (right).*

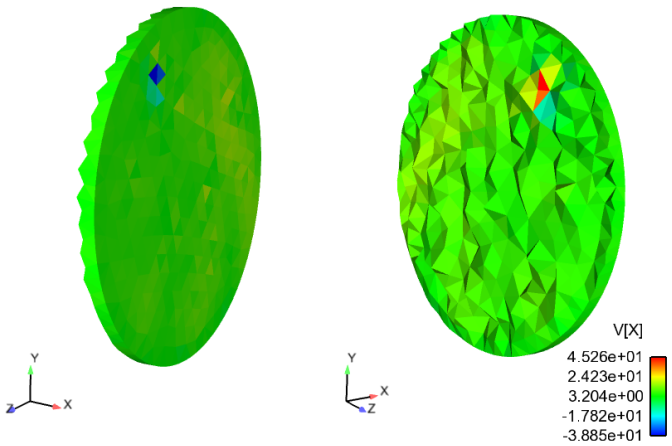

Figure 6.2.4: *Outlet views colored by the axial velocity (V_x).*

6.3 The retained solutions

A 15 hours long run computation represents a simulated time of 1.2 ms and 2.8 ms for the fine mesh and the coarse mesh respectively. Due to some computational problems, the coarse mesh is used to debug the 3-D NSCBC boundary condition instabilities in order to have initial results for the forced flow fields. At the same time, a computation of on the fine mesh is also performed in order to pass the transient behaviour of the flow. The solution to correct the non reflecting boundary condition instability is to apply locally, at the outlet on a small slice, the file *charme_impf*.0 mentioned before. The values of the velocity, the pressure and the temperature are the averaged values of the pressure, the temperature and the velocity in the same slice at the outlet before the correction.

The entropy forcing is performed on the coarse mesh since the convergence is faster but also on the fine mesh. The frequency bandwidth of the entropy forcing is 80 Hz to 600 Hz, ten different frequencies with different phases are injected see Figure 6.3.1. In Figure 6.3.2 on the left hand side, one can see the injected temperature perturbations at the inlet. On the right hand side of the Figure, the zoomed view and the rescale of the temperature bottom limit shows that in the border of this recirculation region, the entropic perturbations are stopped and mixed with the recirculating flow. One can also see that in this region, the injected entropy perturbations are not planar anymore and the planar hypothesis is maybe wrong. One can see in Figure 6.3.3, the Mach number of the nozzle(left hand side) but also a recirculation region upstream of the nozzle (right hand side). In addition, the streamlines of the flow (white) show the real shape of the flow. It seems that due to the recirculation region, the flow does not follow the wall of the geometry.

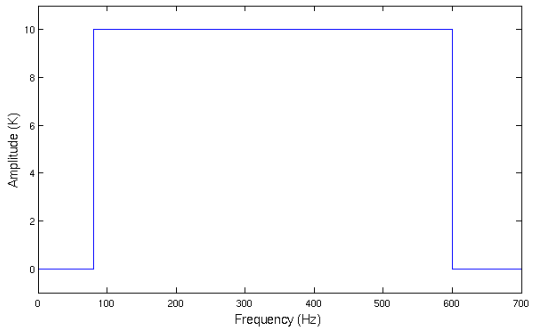

Figure 6.3.1: *Shape of the injected signal.*

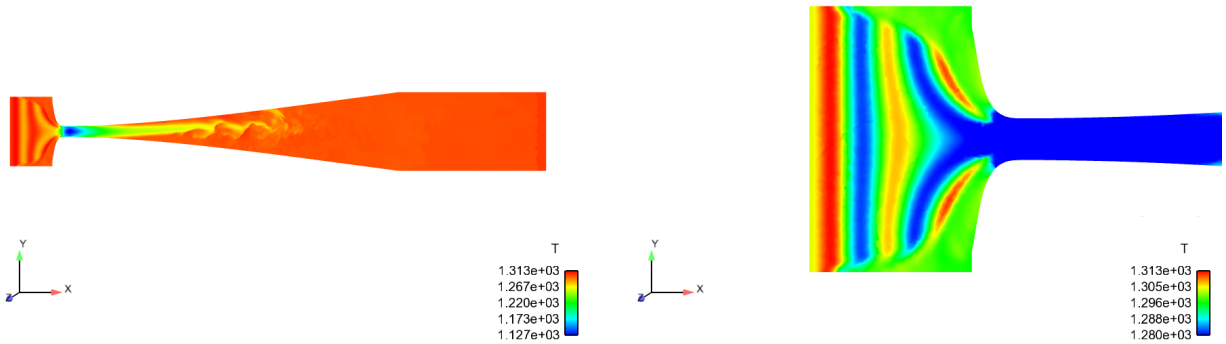

Figure 6.3.2: *Left hand side: Long-cut coloured by temperature. Right hand side: Close-view.*

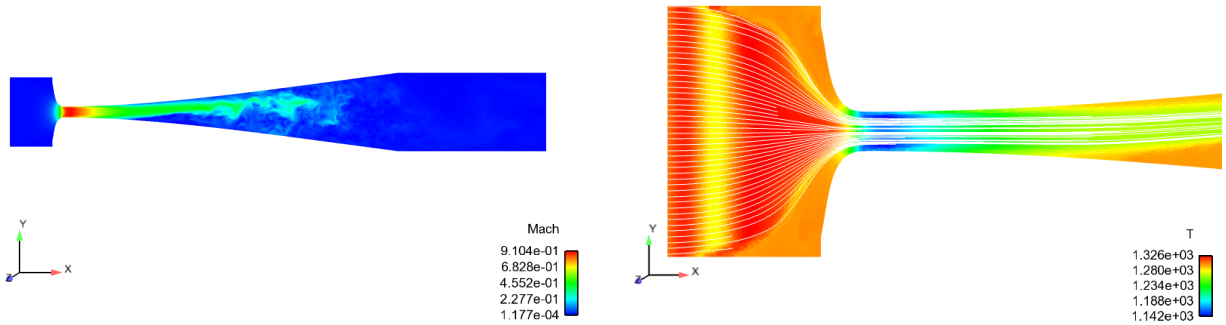

Figure 6.3.3: *Left hand side: Long-cut coloured by Mach number. Right hand side: Long-cut coloured by Temperature with streamlines in white.*

7 Results interpretation and analysis

7.1 Dissipation of the entropic waves upstream of the Nozzle

It is interesting to look at the dissipation over time of the injected perturbations and compare the results with some test cases results available.

7.1.1 Dissipation on the coarse mesh

The dissipation study is performed over 18 runs of 15 hours each. The total physical time is 50.4 ms. The nondimentional temperature fluctuations is defined as $\sigma = \frac{T'}{\bar{T}}$, where T' is the temporal fluctuations of the signal and $\bar{T}$ is the mean temperature during the simulation. In Figure 7.1.2, one can see on the left hand side the nondimentional temperature fluctuations at four different positions or sections see Figure 7.1.1.

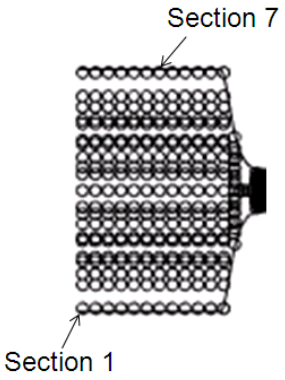

Figure 7.1.1: *Positions of the sections at the inlet.*

In order to study the dissipation, two sections ($Section_1$ and $Section_7$) are used. The distance between the section is 0.0225 m. Knowing the mean speed at the $Section_7$ and the distance between the two sections, a time correction can be applied to match each maximum of the signal (see Figure 7.1.2 on the right hand side). Figure 7.1.3 is a close-up view of the shifted nondimensional temperature fluctuations. Then the difference can be computed and an averaged ratio of the dissipation over time is found using the adimensional temperature fluctuations (σ_1) at $Section_1$ as a reference. The resulting average ratio is 7% see Figure 7.1.4.

The maximum wavelength (when $f = 600$ Hz) is equal to $\lambda_{entropic} = \frac{u}{f_{max}} = \frac{7.59}{600} = 0.01265$ m. The distance is 0.0225 m and thus gives $\frac{0.0225}{0.01265} = 1.77$ wavelengths. This result is compared to the results from where an study of the spatial scheme for the convection transmission in code CEDRE was carried. In our case since the mesh size is 2 mm, the number of points per wavelengths is 6.325. This curves is not present and cannot really be compared to a confidential internal report from Giauque [19]. Nevertheless, the results should be larger than the value given for 16 points par wavelengths for 1.77 turnover times which is around 6%.

This result is valid if the injected wave has only one frequency which is not the case since 10 frequencies between 80 and 600 Hz are injected. One can see in Figure 7.1.5 the discrete Fourier transform of the injected nondimentional temperature fluctuations in the normal and in the log-scale. Nine peaks can be observed meaning that the injected nondimentional temperature fluctuations signals is long enough to separate the different expected frequencies ($\Delta f = \frac{1}{17 \times 0.0028} = 20$Hz). The frequency bandwidth is correct since the signal amplitude drops strongly after 600Hz.

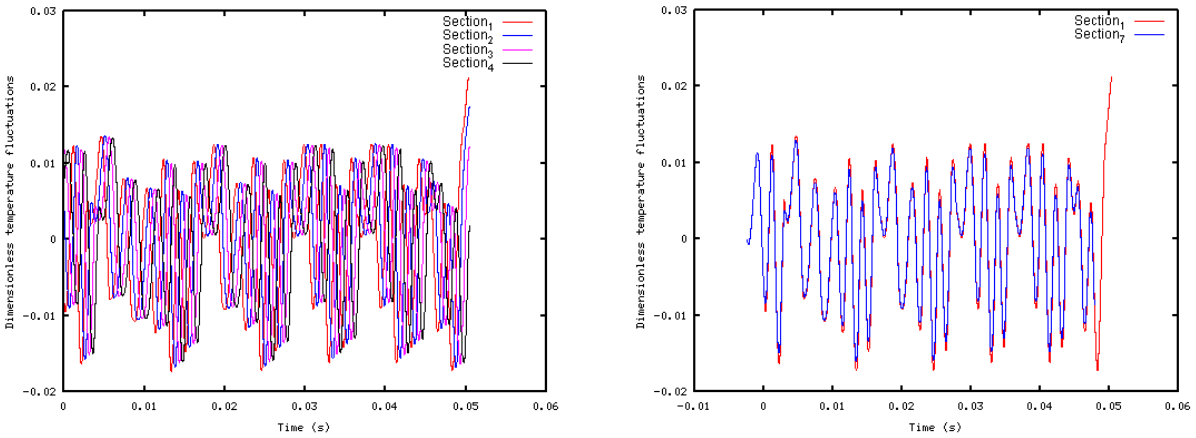

Figure 7.1.2: *Left hand side: adimensional temperature fluctuations at four different positions. Right hand side: superposition of the adimensional temperature fluctuations at σ_1 and the shifted adimensional temperature fluctuations at σ_7.*

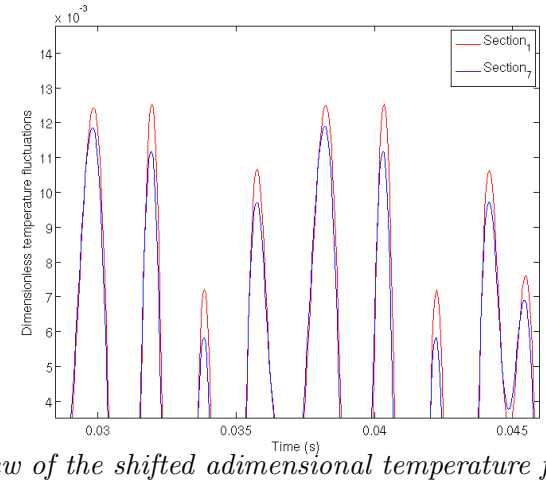

Figure 7.1.3: *Close view of the shifted adimensional temperature fluctuations at σ_7 and σ_1.*

7.1.2 Dissipation on the fine mesh

The same analysis was performed on the fine mesh ($\Delta_x = 0.54$ mm). This mesh size gives 23 points per wavelengths. 17 runs of 15 hours each have been performed and a captured signal is extracted. The total time is 20.4 ms. The general shape signal of the dimensionless temperature fluctuations signal is plotted in Figure 7.1.6 and a close view in Figure 7.1.7.

In Figure 7.1.8, the resulting average ratio (red curve) is 4.83%. Using an interpolation of the results given by 16 and the 32 points per wavelength per from Giauque [19], gives a ratio around 5%. As said previously, this results is valid for a unique frequency which is not true in our case (10 injected frequencies). The dicrete Fourier transform of the forcing signals can be seen in Figure 7.1.9. The signal is too short to separate the frequencies accurately ($\Delta f = \dfrac{1}{17 \times 0.0012} = 49$Hz). But one can see that the injected frequency bandwidth is correct due to the strong drop after 600Hz.

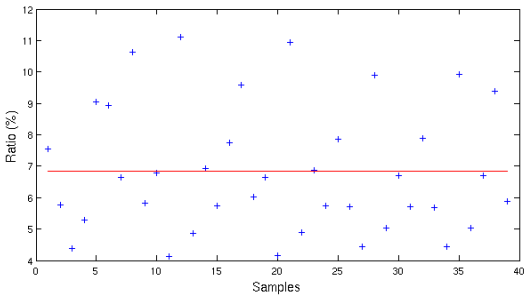

Figure 7.1.4: *Ratio in percentage of the dissipation (blue) and average dissipation ratio (red).*

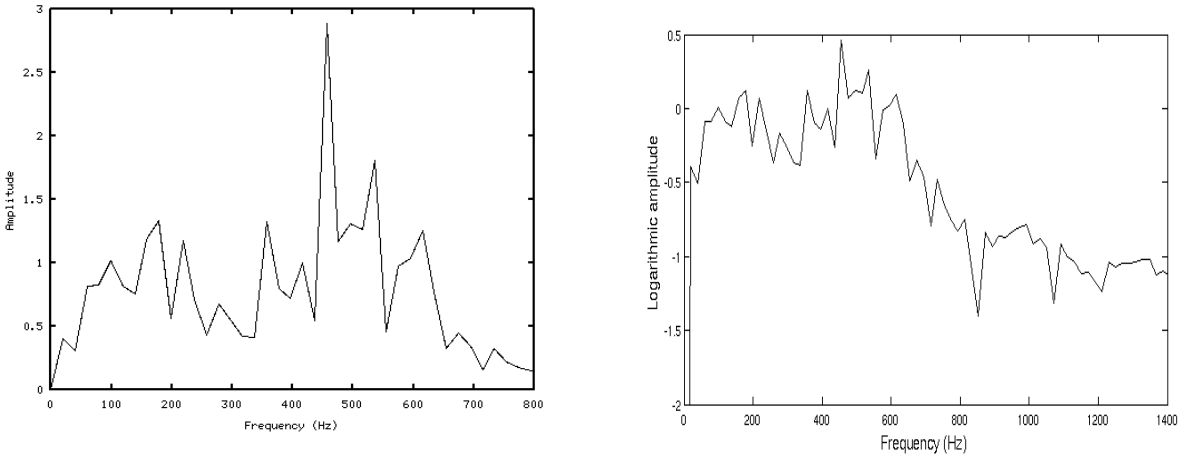

Figure 7.1.5: *Discrete Fourier transform of the normalized temperature fluctuations* σ_1.

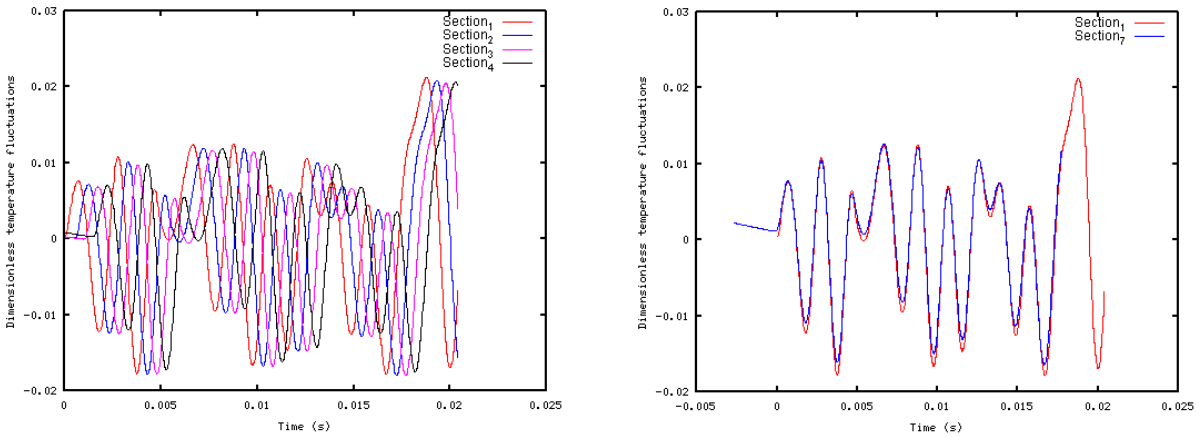

Figure 7.1.6: *Left hand side: adimensional temperature fluctuations at four different positions. Right hand side: superposition of the adimensional temperature fluctuations at* σ_1 *and the shifted adimensional temperature fluctuations at* σ_7.

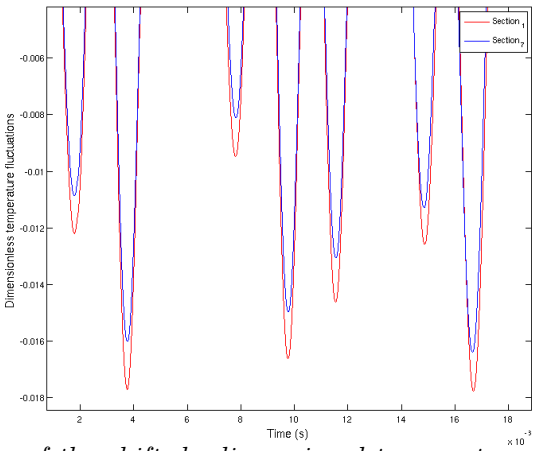

Figure 7.1.7: *Close view of the shifted adimensional temperature fluctuations at σ_7 and σ_1.*

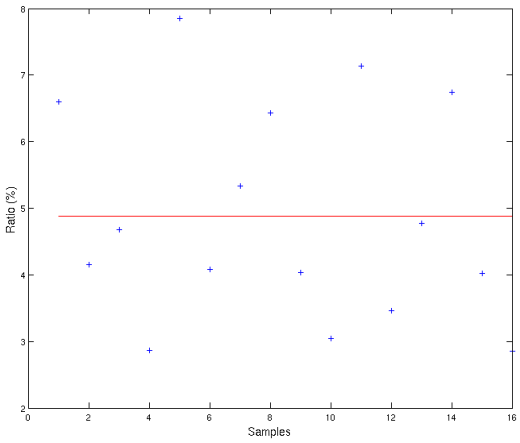

Figure 7.1.8: *Ratio in percentage of the dissipation (blue) and average dissipation ratio (red).*

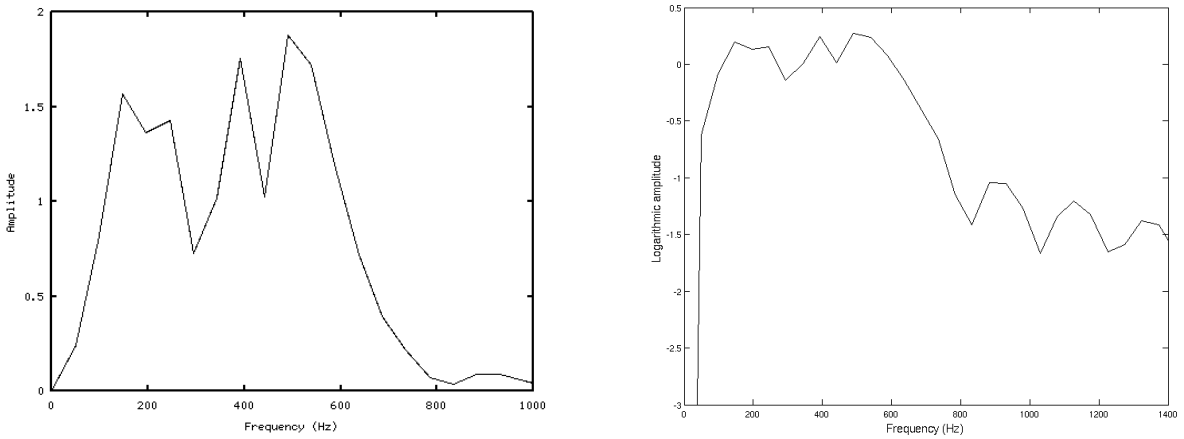

Figure 7.1.9: *Discrete Fourier transform of the normalized temperature fluctuations σ_1.*

7.2 Validation of the post processing created tools

It has been chosen to test and validate the created filtering routines described in Appendix D with artificial signals. The data used to perform this validation are:

- $\rho = 1.22$ kg/m^3 density.
- $C_0 = 340$ m/s sound speed.
- $u = 34$ m/s fluid speed.
- $P = 101325$ Pa.
- $\Delta_x = 0.01$m distance between each points.
- $\Delta_t = 10^{-5}$s time step.
- 3000 time steps giving a 0.03 s length signal.

Two sinus signals have been generated, one moving forward at 210 Hz with a maximum amplitude of 1 Pa and one moving upward at 120 Hz with a maximum amplitude of 1.6 Pa (see Figure 7.2.1). The forward acoustic wave travels at $u + C_0 = 374$m/s and the upward acoustic wave travels at $C_0 - u = 306$m/s.

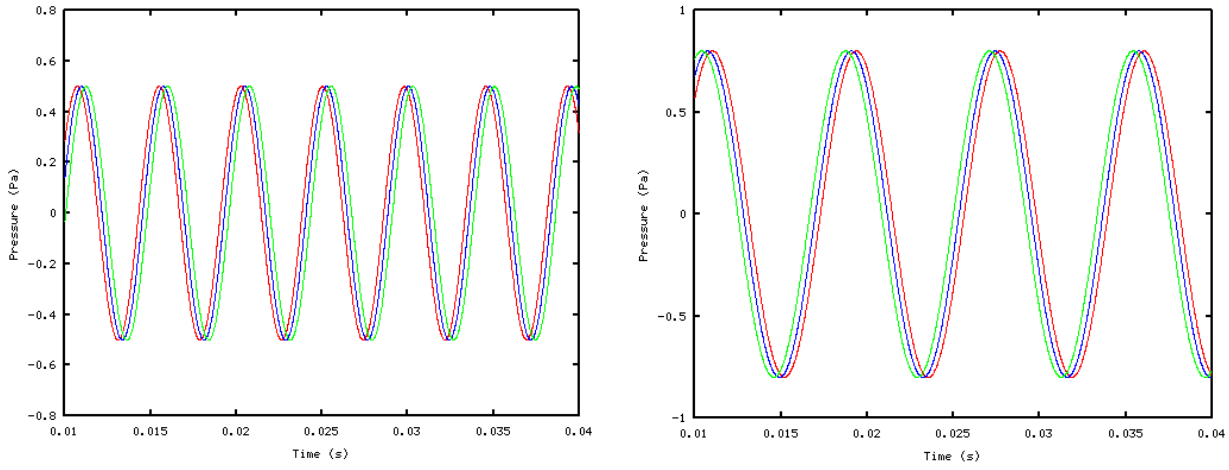

Figure 7.2.1: *Left hand side: forward wave signal. Right hand side: upward wave signal.*

In addition, a stochastic perturbation with a maximum peak to peak amplitude of 1 Pa is also injected. Figure 7.2.2 on the left shows the stochastic perturbation. The final temporal signal which is the sum of the three signals is then propagated spatially over 19 points in the axial direction. In Figure 7.2.2 on the right hand side, the signal which is now time and space dependant is plotted at three different positions. The filtering method codes are then used and the results are shown in Figure 7.2.3. The filtered signals are close to the two created signals even if some temporal fluctuations are still present.

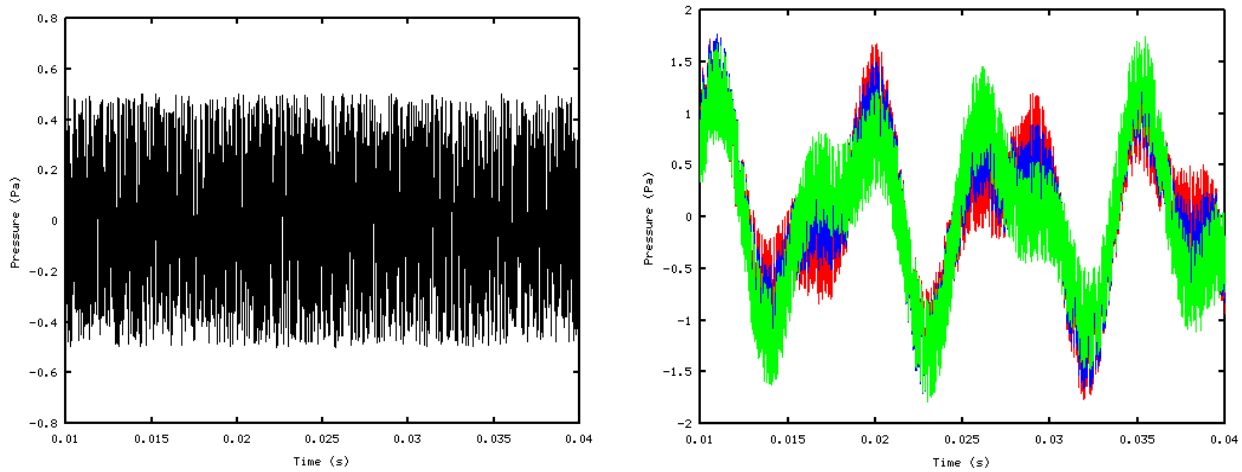

Figure 7.2.2: *Left hand side: Turbulent pressure signal. Right hand side: Final obtained signal at* $Point_1$ *(red),* $Point_{10}$ *(blue) and* $Point_{20}$ *(green).*

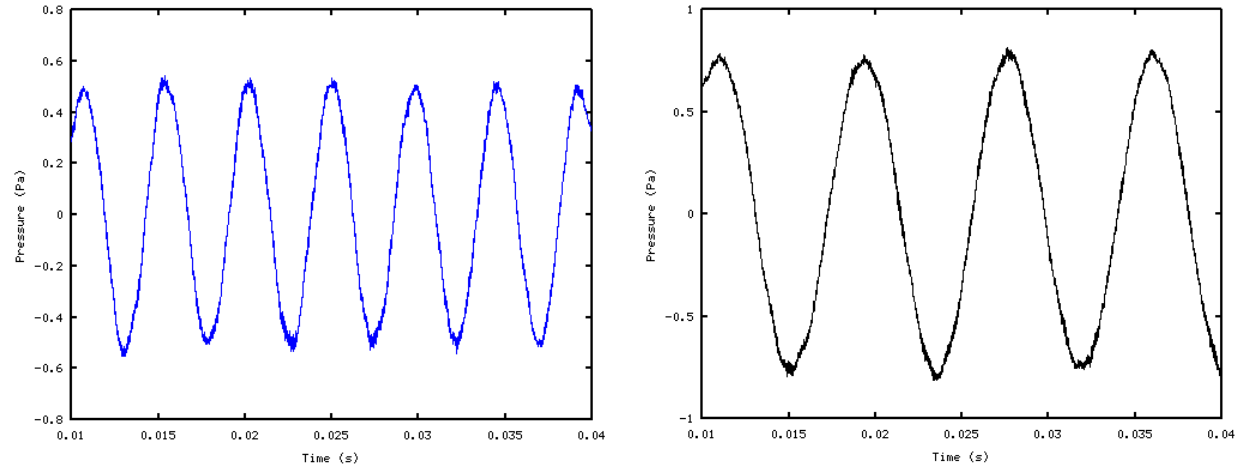

Figure 7.2.3: *Results of the filtering method for the forward signal (left) and the upward signal (right).*

Finally, the SPL (Sound Pressure level) or sound level L_p is calculated. The unit of this measure is expressed in dB. It is defined as follows:

$$L_p = 10 * log_{10}\left(\frac{P_{rms}^2}{P_{ref}^2}\right) \text{ where } P_{ref} = 20\mu\text{Pa} \tag{7.2.1}$$

where $P_{ref} = 20$ µPa is considered as the threshold for human hearing. The discrete Fourier transform of the filtered signals can be seen in Figure 7.1.5 and the results are closed to the injected one, the filtering routines are performing well.

7.3 Application of the post processing tools to the nozzle flow resolved on the coarse mesh

7.3.1 Correction of the signal deviation

During the 50.4 ms of the entire simulation, a drift of the upstream mean pressure has been detected. The pressure difference is around 600 Pa (from 227478 Pa to 228115 Pa between the beginning and

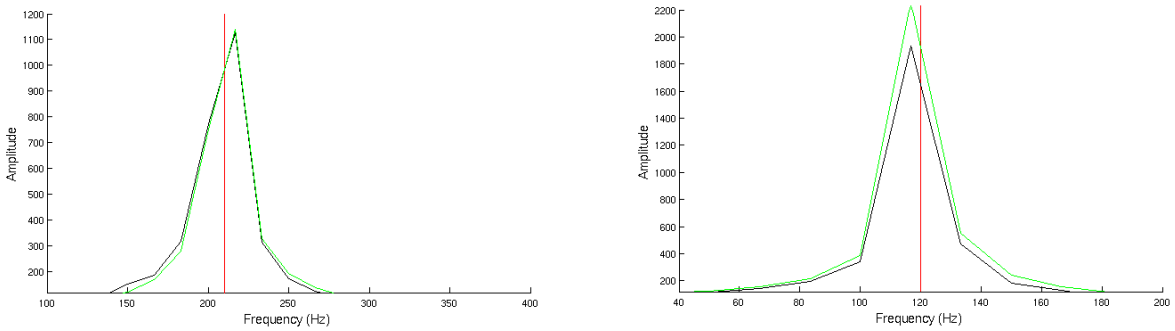

Figure 7.2.4: *Discrete Fourier Transform of the Filtered signals of the forward wave (blue) and the upward wave (black), the red lines are the frequency of the injected signals.*

the end of the simulation. This represents an increase of 0.27%. In Figure 7.3.1, one can see the normalized pressure fluctuation deviation but also that this drift seems to be linear. This deflection will pollute our spectral analysis since it occurs at low frequencies. In order to get rid of this deviation, the signals are corrected by subtracting this linear increase. This correction is obtained by dividing the difference between the final pressure and the initial pressure by the simulated time. In Figure 7.3.2, one can see the shape of the corrected signals. The reason of this drift is maybe because the systems seems to be not fully converged.

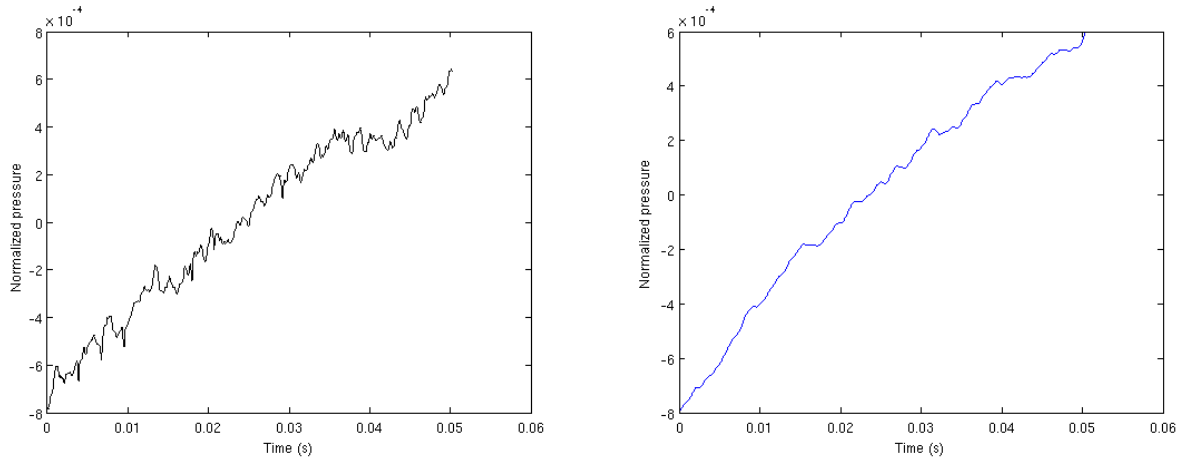

Figure 7.3.1: *Filtered signals of the upstream wave (black) and the downstream wave (blue).*

7.3.2 The non reflective boundary conditions

The correlation method applied to the acoustic field is a good way investigate reflection patterns, the two acoustic waves are being closely related to each other. The auto-correlation coefficient in Figure 7.3.3 are represented in blue (P^+) or in black (P^-). Their shapes in this case confirms that when the time delay is zero, the signal is correlated with itself. The curve in red is the cross-correlation between an upstream acoustic wave and a downstream acoustic wave at the same location. The different curves are shown in Figure 7.3.3 at different positions. Close to the Inlet at $Section_1$ (left hand side of Figure 7.3.3), one can see that those signals are not strongly correlated. In addition knowing the mean speed at this position and the distance between the inlet and $Section_1$, one can compute the time needed for the wave to make a round trip from $Section_1$ to the Inlet. In our case, this time should be $t = \frac{0.00125}{701.43+7.58} + \frac{0.00125}{701.43-7.58} = 3.56 \times 10^{-6}$ s. On the left hand side of the Figure

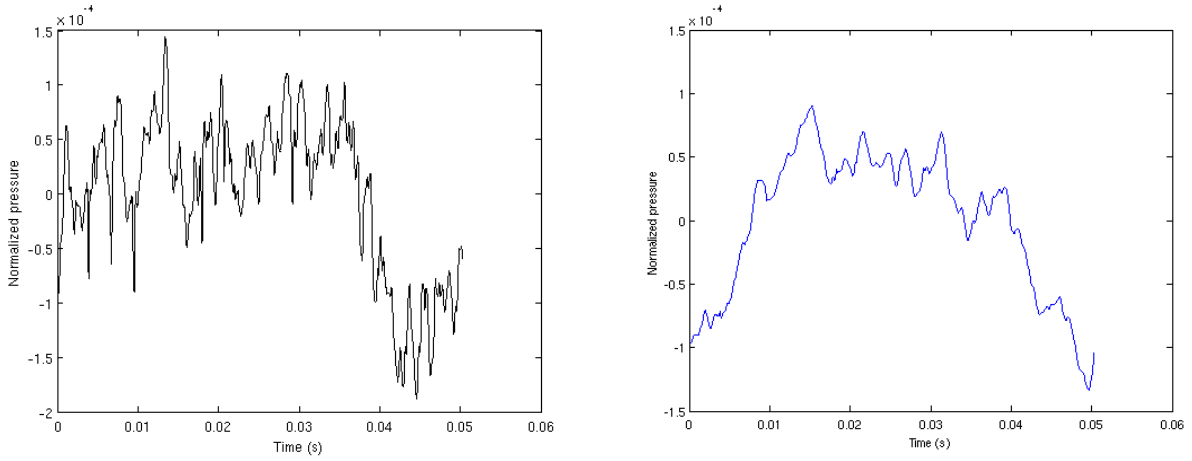

Figure 7.3.2: *Correction of the filtered signals of the upstream acoustic wave (black) and the downstream acoustic wave (blue).*

7.3.3, close to zero, there is not a peak that shows the correlation being stronger. The same analysis can be performed on the downstream acoustic wave. The position will be this time $Section_{21}$, located close to the outlet of the nozzle. Knowing the distance between this position and the Outlet, the time for an acoustic wave to make a round trip should be $t = \frac{0.15}{701.85+8.46} + \frac{0.15}{701.85-8.46} = 4.28 \times 10^{-4}$ s. On the right hand side of Figure 7.3.3, no peak can be seen either for this time delay. As a conclusion, it seems that the non reflective boundary conditions perform well. No phase drift on the inter correlation curve shows that the signals are not strongly correlated.

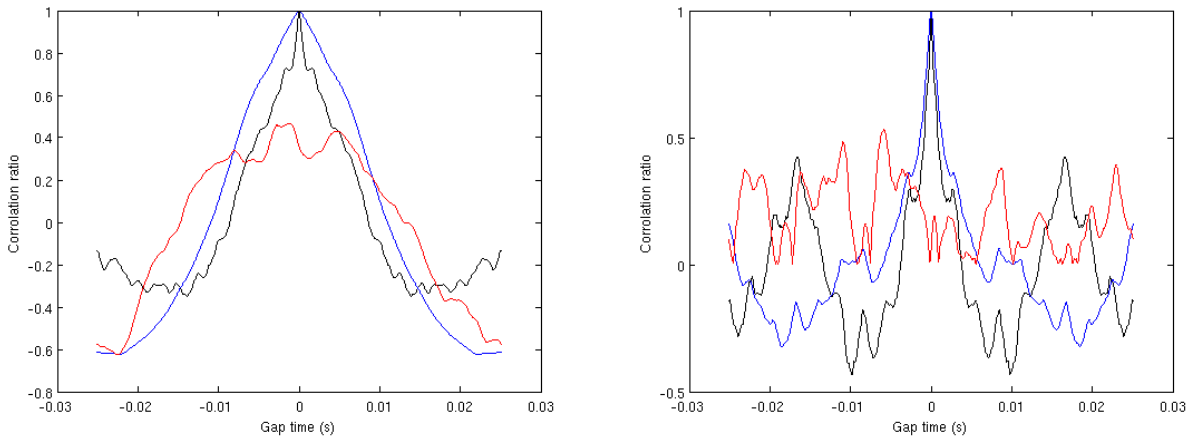

Figure 7.3.3: *Auto- and cross-correlations of the upstream acoustic waves (left and the downstream acoustic waves right. Black: auto-correlation of the upward wave, Blue: auto-correlation of the forward wave, Red line: cross-correlation between the upward and the forward waves.*

7.3.3 Transfer functions

The transfer functions are computed in the spectral domain. In this study, F_1 and F_2 can be seen respectively as the conversion ratio of the injected entropy fluctuations into upstream and downstream acoustic perturbations. These transfer functions are expressed as the following using Marble & Candel

[31]:

$$F_1 = \frac{P_1^{-*}}{\sigma}$$
$$F_2 = \frac{P_2^{+*}}{\sigma}$$

where

$$P_1^{-*} = \frac{P_1^{-'}}{\overline{P_1}} = \frac{p_1^{'} - \rho c u_1^{'}}{2 \times \overline{P_1}}$$
$$P_2^{+*} = \frac{P_2^{+'}}{\overline{P_2}} = \frac{p_2^{'} + \rho c u_2^{'}}{2 \times \overline{P_2}}$$

One can see in Figure 7.3.4, the transfer functions of F_1 and F_2 using a discrete Fourier transform. It is difficult to interpret the results because many peaks related to the Fourier transform method applied to short time signals. The maximum entropy method is therefore used in the following. The maximum entropy density approach is based on the efficient use of available information, which is interesting since the signal is short in time. It is obtained by maximizing Shannon's (1948) entropy measure. It is possible to choose the degree of the autoregressive model used (see Figures 7.3.5). An order of five seems to be good as the curves have the same trend if the order becomes higher. Only the point at $x = 0$ increases as the order increases.

The obtained transfer function are compared with results from MARCAN (green curves), which is an Analytical solver based on the equation formulated by Marble & Candel [31] and solved by considering the nozzle as a collection of elementary units in which the velocity evolves linearly. The results shows that upstream of the nozzle, the amplitude of the transfer function of the nozzle is larger than the analytical results. The same trend can be observed on the downstream transfer function, which appears to have even higher amplitude. Note that for F_1 at 400Hz,the amplitude of the transfer function is arround the same order of magnitude. In Figure 7.3.6, one can see that for F_2 the amplitude is four times higher than the analytical value.

The presence of a jet in the divergent part of the nozzle might be the reason for such a difference. A modification of the geometry might avoid the jet to appear by reducing the expansion angle of the divergent part of the nozzle.

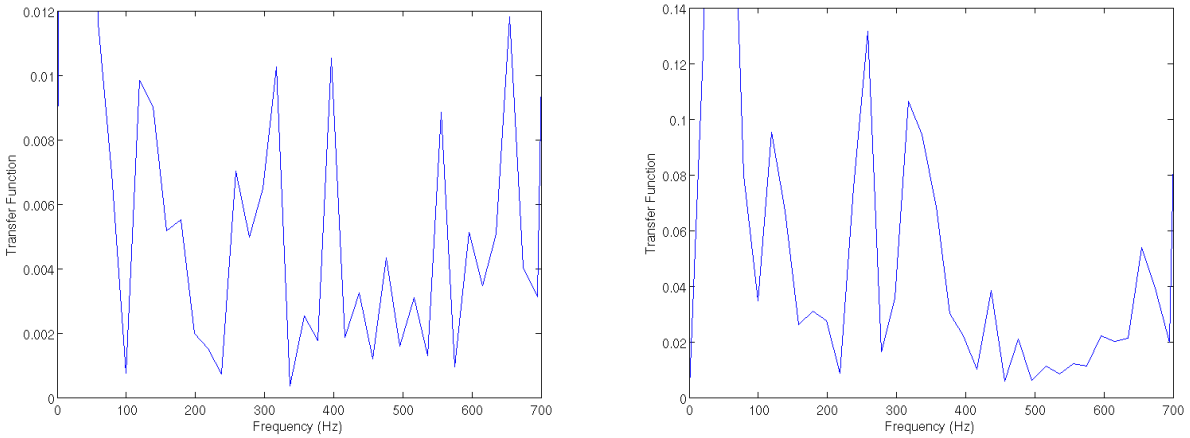

Figure 7.3.4: *Close view of the transfer function of F_1 and F_2.*

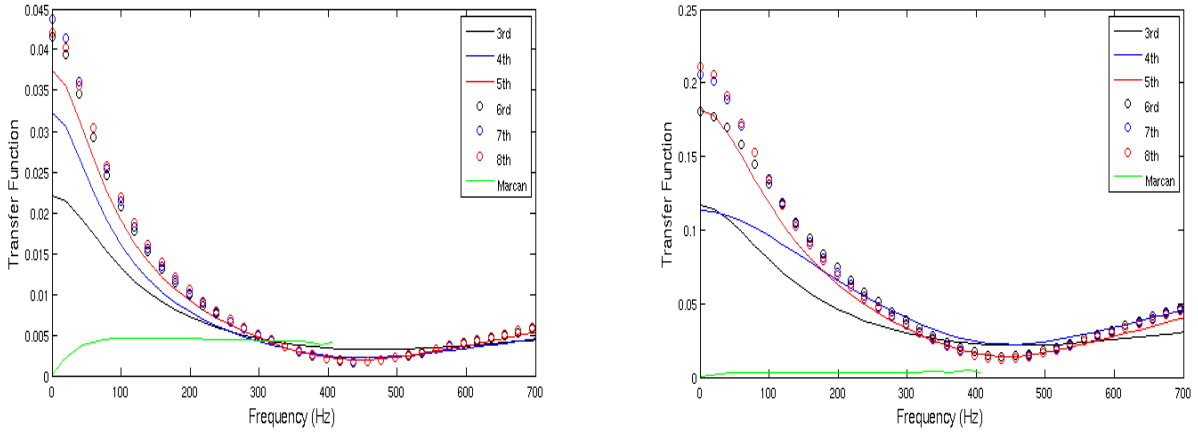

Figure 7.3.5: *Left hand side: Upstream transfer function F_1 using the maximum entropy method for different orders of the autoregressive model. Right hand side: Downstream transfer function F_2 using the maximum entropy method for different orders of the autoregressive model.*

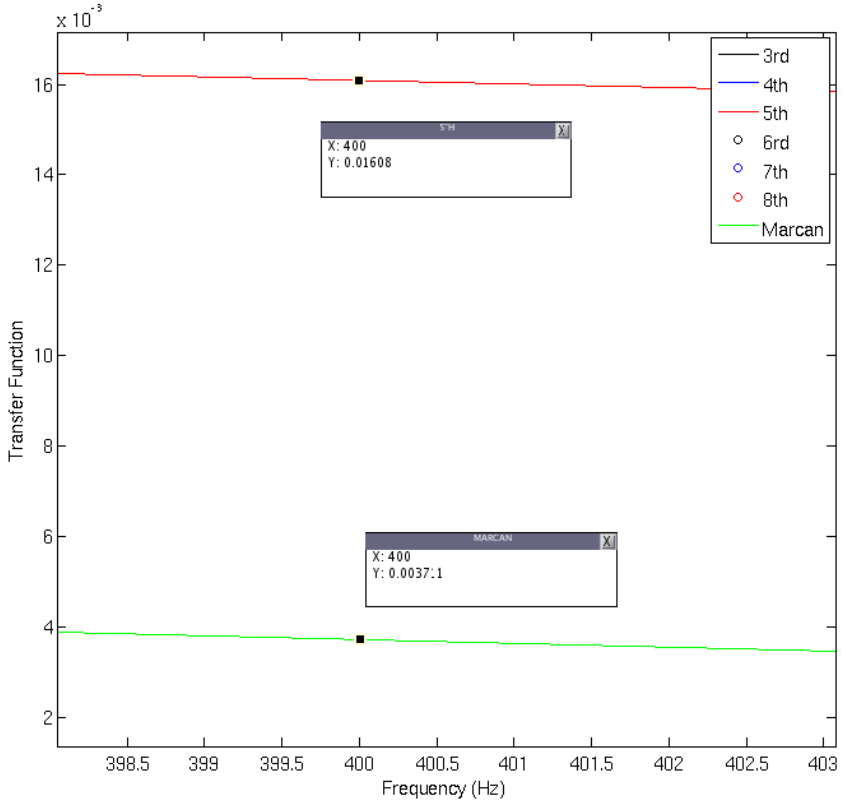

Figure 7.3.6: *Close view of F_2 at 400*Hz.

Conclusion of the study

During the last two decades, aerodynamic noise sources appearing in the vicinity of aircraft engines (fan and jet noise) have been significantly reduced. Consequently, the noise emission from the core engine components is now gaining in relative importance especially during the take-off and landing phases when the operating conditions are not at their optimum. Core noise has two main origins. Direct noise is generated by unsteady heat release fluctuations at the flame front in the combustion chamber. Indirect noise is induced by the acceleration of burnt gas heterogeneities both in velocity (vorticity) and temperature (entropy waves). A brief review on both types of combustion noise is first proposed.

The context of the subject and the objectives are then described and the numerical simulation of the Discern Nozzle test bench has been performed. Due to the extreme operating conditions (high pressure and temperature gradients), it is still difficult to control the desired evolution of the system. In our case, the variation of Mach number flow impairs the generality of the present results. In addition, this study shows that the 1-D approach used for the generation of the nozzle geometry is not enough. Indeed, the 3-D effects change the flowfield and the flow does not follow the wall of the nozzle. The creation of the boundary layer changes the position of the theoretical and the real throat. Also some stability problems due to the Navier-Stokes Characteristic Boundary Conditions implementation are reported. The boundary condition are quite recent in CEDRE and an alternative solution was used to correct this issue and obtain some results. The debuging of the problem will be performed soon.

The preliminary results of 17 forced calculations for the fine mesh and 18 for the coarse mesh give a first overview of the flow field behaviour. A validation of the post-processing tools is first done and the results showed that the filtering method performs well.

The non reflective boundary condition behaviour is also investigated thanks to the analysis of the auto and cross correlation coefficient of the acoustic waves in the nozzle. The acoustic transfer functions of the Discern Nozzle under an entropy forcing is computed for the coarse mesh. It appears that the generated noise is of much higher amplitude than expected. The presence of a jet in the divergent part of the nozzle might strongly affect the acoustic response of the system because of numerous turbulent structures.

A modification of the geometry could be beneficial in that it would enable the analysis of the indirect noise without any other acoustic source being present. This could be done by reducing the expansion angle in the divergent thereby increasing slightly the overall size of the system.

This analysis will be continued during the last month of the internship but also during the beginning of a PhD. The geometry followed by the flow will be interpolated and the corresponding transfer functions given by the analytical solver MARCAN will be compared to our results. Finally another way to compute the acoustic transfer function will also be investigated. The Wiener-Hopf relation will be studied to solve the Wiener-Hopf equation and give the optimal Wiener filter. The transfer functions will then be compared with results provided by the Analytical solver and the Euler 1-D solver.

References

[1] C. Bailly, C. Bogey, and S. Candel. "Modelling of sound generation by turbulent reacting flows". In: *International Journal of Aeroacoustics, Vol. 9* (2010), pp. 461–490.

[2] F. Bake, N. Kings, and I. Roehle. "Fundamental mechanism of entropy noise in aero-engines: experimental investigation". In: *Journal of Engineering for Gas Turbines and Power, Vol 130* (2008), pp. 1 –6.

[3] F. Bake, U. Michel, and I. Roehle. "Investigation of Entropy Noise in Aero-Engine Combustors". In: *Journal of Engineering for Gas Turbines and Power, Vol. 129* (2007), pp. 370–376.

[4] F. Bake et al. "Experimental investigation of the entropy noise mechanism in aero-engines". In: *International Journal of Aeroacoustics, Vol 8* (2009), pp. 125–142.

[5] F. Bake et al. "Indirect Combustion Noise: Investigations of Noise Generated by the Acceleration of Flow Inhomogeneities". In: *Workshop BRUCO, Ecole Centrale Paris* (2009).

[6] C. Bender and H. Büchner. "Combustion noise from non -premixed and lean-premixed swirl flames". In: *Acta acustica united with acustica, Vol 95* (2009), pp. 402–408.

[7] A. L. Birbaud and H. Pitsch. "Combustion noise modeling using compressible simulations". In: *Center for Turbulence Research, Annual Research Briefs* (2008).

[8] A. W. Bloy. "The pressure waves produced by the convection of temperature disturbances in high subsonic nozzle flows". In: *Journal of Fluid Mechanics, Vol. 94, part 3* (1979), pp. 465–475.

[9] M. S. Bohn. "Response of a subsonic nozzle to acoustic and entropy disturbances". In: *Journal of Sound and Vibration, Vol. 52* (1977), pp. 283–297.

[10] S. L. Bragg. "Combustion noise". In: *Journal of Institute of Fuel, Vol. 36* (1963), pp. 12–16.

[11] S. Candel et al. "Flame dynamics and combustion noise: progress and challenges." In: *International Journal of Aeroacoustics, Vol. 8* (2009), pp. 1–56.

[12] F. Chedevergne. "Advanced wall model for aerothermodynamics". In: *International Journal of Heat and Fluid Flow, Vol. 31* (2010), pp. 916–924.

[13] P. Chevalier et al. "CEDRE: development and validation of a multiphysic computational software". In: *1st EUCASS, Moscow* (2005).

[14] B. Chu and L. S. G. Kovàsznay. "Non-linear interactions in a viscous heat-conductiong compressible gas". In: *Journal of Fluid Mechanics, Vol. 3* (1957), pp. 494–514.

[15] N. A . Cumpsty and F.E. Marble. "The generation of noise by the fluctuations in gas temperature into a turbine". In: *University of Cambrigde Report No. CUED/ATURBO/TR 57* (1974).

[16] N. A . Cumpsty and F.E. Marble. "The Interaction of entropy fluctuations with turbine blade rows; a mechanism of turbojet engine". In: *Proceedings of the Royal Society of London, Series A, Vol. 357* (1977), pp. 323–344.

[17] A. Dowling. "Thermoacoustics and instabilities". In: *Modern methods in analytical acoustics. Crighton et al. (eds), Springer-Verlag* (1992).

[18] S. Ducruix. "Programme blanc, projet DISCERN". In: *ANR document scientifique* (2011).

[19] A. Giauque. "PRF MAMBO: Etude Numérique du Bruit de Combustion Indirect dans une Tuyère Idéalisée". In: (2009).

[20] A. Giauque and M. Huet. "Analytical analysis of indirect combustion noise in subcritical nozzles". In: *Proceedings of ASME Turbo Expo 2012* (2012).

[21] M.S. Howe. "Indirect combustion noise". In: *Journal Fluid Mechanic, Vol. 659* (2010), pp. 267–288.

[22] J.C.R Hunt, A.A. Wray, and P. Moin. "Eddies, stream and convergence zone in turbulent flows". In: *Center for turbulence research report, CTR-S88* (1988).

[23] S. Kaji and T. Okazaki. "Propagation of sound waves through a blade row I, Analysis based on the semi-actuator disk theory". In: *Journal of Sound and Vibration, Vol. 11* (1970), pp. 339–353.

[24] S. Kaji and T. Okazaki. “Propagation of sound waves through a blade row II, Analysis based on the semi-actuator disk theory”. In: *Journal of Sound and Vibration, Vol. 11* (1970), pp. 355–375.
[25] Jan Kopitz. “Characteristics-based filter identification of planar acoustic waves in numerical simulation of turbulent compressible flow”. In: *12th international congress on sound and vibration* (2005).
[26] A. Lamraoui et al. “Experimental investigation of combustion noise from a swirled turbulent flame”. In: *Workshop BRUCO, Ecole Centrale Paris* (2009).
[27] B. van Leer. “Towards the ultimate concervative difference scheme. V. A second order sequel to Gudonov’s method”. In: *Journal of Computational Physics, Vol. 32* (1979), 101–136.
[28] M. Leyko et al. “Combustion noise in aero-engines”. In: *Workshop BRUCO, Ecole Centrale Paris* (2009).
[29] M. Leyko et al. “Numerical and analytical investigation of the indirect noise in a nozzle”. In: *Compte rendu de Mécanique, Vol. 337* (2009), pp. 415–425.
[30] G. Lodato, P. Domingo, and L. Vervisch. “Three-dimensional boundary conditions for direct and large-eddy simulation of compressible viscous flows”. In: *Journal of Computational Physics, Vol. 227* (2008), 5105–5143.
[31] F.E Marble and S. M. Candel. “Acoustic disturbance from gas non-uniformities convected through a nozzle”. In: *Journal of Sound and Vibration, Vol. 55* (1977), pp. 225–243.
[32] C. E. Martin, L. Benoit, and Y. Sommerer. “Large-Eddy Simulation and acoustic analysis of a swirled staged turbulent combustor”. In: *AIAA Journal Vol. 44* (2006).
[33] W. H. Moase, M. J. Brear, and C. Manzie. “The forced response of choked nozzles and supersonic diffusers”. In: *Journal of Fluid Mechanics, Vol. 585* (2007), pp. 281–304.
[34] B. Mühlbauer, B. Noll, and M. Aigner. “Fundamental mechanism of entropy noise in aero-engines”. In: *Acta Acustica united with Acustica, Vol. 95* (2009), pp. 470–478.
[35] R. S. Muir. “The application of a semi-actuator disk model to sound transmission calculations in turbomachinery part I: the single blade row”. In: *Journal of Sound and Vibration, Vol. 54* (1977), pp. 393–408.
[36] R. S. Muir. “The application of a semi-actuator disk model to sound transmission calculations in turbomachinery part II: multiple blade rows”. In: *Journal of Sound and Vibration, Vol. 55* (1977), pp. 355–349.
[37] ONERA. “CEDRE 4.2, Présentation de la chaine de calculs CEDRE”. In: (2012).
[38] G. F. Pickett. “Core engine noise due to temperature fluctuations convecting through turbine blade rows”. In: *2nd Aeroacoustics Conference, AIAA Paper, AIAA 75-528* (1975).
[39] T.J. Poinsot and S.K. Lele. “Boundary conditions for direct simulations of compressible viscous flows”. In: *Journal of Computational Physics, Vol. 101* (1992), pp. 104–129.
[40] G. Rahier et al. “Comparative jet noise computations using a coupled CFD-acoustic”. In: *11 TH International congress on Sound and Vibrations, Saint Petersbourg* (2004).
[41] C. Richter, L. Panek, and F. Thiele. “On the application of CAA - Methods for the simulation of indirect combustion noise”. In: 11^{th} *AIAA/CEAS Aeroacoustics Conference, AIAA Paper, AIAA 2005-2919* (2005).
[42] C. Richter and F. Thiele. “Zonal approaches for the simulation of indirect combustion noise”. In: *19th International Congress and Acoustics* (2007).
[43] Y. Saad and M. H. Schultz. “GMRES: A generalized minimal residual algorithm for solving nonsymmetric linear systems”. In: *Journal on Scientific and Statistical Computing, Vol. 7* (1986), pp. 856–869.
[44] C. Silva, M. Leyko, and F. Nicoud. “Using LES and linear solver assess direct combustion noise”. In: *Workshop BRUCO, Ecole Centrale Paris* (2009).
[45] W. C. Strahle. “On combustion generated noise”. In: 7^{th} *AIAA/SAE Propulsion Joint Specialist Conference, AIAA Paper* (1971), pp. 71–735.

[46] A. Thomas and G. T. Williams. “Flame noise: sound emission from spark-ignited bubbles of combustible gas”. In: *Proceedings of the Royal Society of London, Series A, Vol. 294* (1966), pp. 449–446.

Appendices

A Derivations

A.1 Continuity Equation 2.2.1

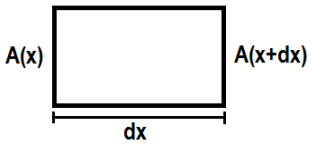

A stands for the sectional area and assuming c_p is constant, $\nu = 0$ no viscous effect. From the mass conservation equation :

$$\begin{aligned}
\int_A \frac{\partial \rho}{\partial t}\,\mathrm{d}V &= (\rho u A)(x) - (\rho u A)(x+dx) \\
A\frac{\partial \rho}{\partial t}dx &= [\rho u A](x) - [\rho u A](x+dx) \\
A\frac{\partial \rho}{\partial t} &= \frac{[\rho u A](x) - [\rho u A](x+dx)}{dx} \\
A\frac{\partial \rho}{\partial t} &= -\frac{\partial(\rho u A)}{\partial x} \\
A\frac{\partial \rho}{\partial t} &= -A\frac{\partial(\rho u)}{\partial x} - \rho u\frac{\partial A}{\partial x} \\
\frac{1}{\rho}\left(\frac{\partial \rho}{\partial t} + \frac{\partial(\rho u)}{\partial x}\right) &= -\frac{u}{A}\frac{\partial A}{\partial x}
\end{aligned}$$

A.2 Momentum Equation 2.2.2

It is assumed a material volum V(t), the mass contained in this volume is:

$$m = \int_{V(t)} \rho dV$$

If the material volume does not contain sources, the mass is constant so:

$$\frac{dm}{dt} = \frac{d}{dt}\int_{V(t)} \rho dV = 0$$

Applying the transport theorem on V(t):

$$\begin{aligned}
\frac{d}{dt}\int_{V(t)} \rho dV &= \int_{V(t)} \frac{\partial \rho}{\partial t} dV + \int_{A(t)} \rho v.n dA \\
0 &= \int_{V(t)} \frac{\partial \rho}{\partial t} dV + \int_{A(t)} \rho v.n dA
\end{aligned}$$

If the volume V(t) does not contain a discontinuity's surface and thanks to the theorem of Green-Ostragradsky, one can write:

$$\int V(t) = [\frac{\partial \rho}{\partial t} + \nabla.\rho u]dV = 0$$

The volume of integration is arbitrary and thus the integral has to be nul:

$$0 = \frac{\partial \rho}{\partial t} + \nabla \rho v$$

A.3 Entropy Equation 2.2.3

$$\frac{s}{c_p} = \ln \frac{p^{\frac{1}{\gamma}}}{\rho}$$

$$\frac{p^{\frac{1}{\gamma}}}{\rho} = \exp(\frac{s}{c_p})$$

$$\frac{p^{\frac{1}{\gamma}}}{\rho} \exp(\frac{-s}{c_p}) = 0$$

$$\frac{D}{Dt}\left(\frac{p^{\frac{1}{\gamma}}}{\rho} \exp(\frac{-s}{c_p})\right) = 0$$

$$\frac{p^{\frac{1}{\gamma}}}{\rho}\frac{D}{Dt}\left(\exp(\frac{-s}{c_p})\right) + \exp(\frac{s}{c_p})\frac{D}{Dt}\left(\frac{p^{\frac{1}{\gamma}}}{\rho}\right) = 0, \text{but } \frac{p^{\frac{1}{\gamma}}}{\rho} \text{ is constant since the flow is isentropic so } \frac{D}{Dt}\frac{p^{\frac{1}{\gamma}}}{\rho} = 0$$

$$\text{thus } \frac{p^{\frac{1}{\gamma}}}{\rho}\frac{D}{Dt}\left(\exp(\frac{-s}{c_p})\right) = 0$$

$$\text{and finally } \frac{\partial s}{\partial t} + u\frac{\partial s}{\partial x} = 0$$

A.4 Simplified continuity Equation 2.2.5

The mass conservation is written:

$$\frac{1}{\rho}\left(\frac{\partial \rho}{\partial t} + \rho\frac{\partial u}{\partial x} + u\frac{\partial \rho}{\partial x}\right) = -\frac{u}{A}\frac{\partial A}{\partial x}$$

using small perturbations of the variables: $p = \bar{p}\left(1 + \frac{p'}{\bar{p}}\right)$, $\rho = \bar{\rho}\left(1 + \frac{\rho'}{\bar{\rho}}\right)$, $u = \bar{u}\left(1 + \frac{u'}{\bar{u}}\right)$ and $s = \bar{s}\left(1 + \frac{s'}{\bar{s}}\right)$. The Equation above can be rewritten:

$$\frac{1}{\bar{\rho}}\frac{\partial \bar{\rho}}{\partial t} + \frac{1}{1 + \frac{\rho'}{\bar{\rho}}}\frac{\partial(\frac{\rho'}{\bar{\rho}})}{\partial t} + \bar{u}\left(1 + \frac{u'}{\bar{u}}\right)\left(\frac{1}{\bar{\rho}}\frac{\partial \bar{\rho}}{\partial x} + \frac{1}{1 + \frac{\rho'}{\bar{\rho}}}\frac{\partial(\frac{\rho'}{\bar{\rho}})}{\partial x}\right)$$

$$+\bar{u}\left(1 + \frac{u'}{\bar{u}}\right)\frac{\partial \bar{u}}{\partial x} + \bar{u}\frac{\partial(\frac{u'}{\bar{u}})}{\partial x} = -\frac{\bar{u}}{A}\frac{\partial A}{\partial x} - \frac{u'}{A}\frac{\partial A}{\partial x}$$

using Equation 2.2.3 and by developing those terms to first order using $\frac{1}{1+\alpha} \simeq 1-\alpha$ and neglecting second order terms, this equation can be simplified to:

$$\frac{\partial(\frac{\rho'}{\bar{\rho}})}{\partial t} + \frac{u'}{\bar{\rho}}\frac{\partial \bar{\rho}}{\partial x} + \bar{u}\frac{\partial(\frac{\rho'}{\bar{\rho}})}{\partial x}) + \frac{u'}{\bar{u}}\frac{\partial \bar{u}}{\partial x} + \bar{u}\frac{\partial(\frac{u'}{\bar{u}})}{\partial x} = -\frac{u'}{A}\frac{\partial A}{\partial x}$$

Applying the mass conservation equation and $s'/c_p = (s'/c_p)(t - \int^x d\zeta/u)$:

$$\frac{\partial(\frac{p'}{\gamma\bar{p}})}{\partial t} - \frac{\partial(\frac{s'}{c_p})}{\partial t} + \bar{u}\frac{\partial(\frac{p'}{\gamma\bar{p}})}{\partial x} - \bar{u}\frac{\partial(\frac{s'}{c_p})}{\partial x} + \bar{u}\frac{\partial(\frac{u'}{\bar{u}})}{\partial x} = 0$$

Finally, with the relation of isentropy (Equation (21)):

$$\frac{\partial(\frac{p'}{\gamma\bar{p}})}{\partial t} + \bar{u}\frac{\partial(\frac{p'}{\gamma\bar{p}})}{\partial x} + \bar{u}\frac{\partial(\frac{u'}{\bar{u}})}{\partial x} = 0$$

A.5 Simplified momentum Equation 2.2.6

From the momentum Equation 2.2.2:

$$\frac{\partial u}{\partial t} + u\frac{\partial u}{\partial x} + \frac{1}{\rho}\frac{\partial p}{\partial x} = 0$$

Using small perturbations of the variables $p = \bar{p}\left(1 + \frac{p'}{\bar{p}}\right)$, $\rho = \bar{\rho}\left(1 + \frac{\rho'}{\bar{\rho}}\right)$, $u = \bar{u}\left(1 + \frac{u'}{\bar{u}}\right)$ and $s = \bar{s}\left(1 + \frac{s'}{\bar{s}}\right)$. The equation can be rewritten as:

$$\bar{u}\frac{\partial\left(1+\frac{u'}{\bar{u}}\right)}{\partial t} + \left(1+\frac{u'}{\bar{u}}\right)\frac{\partial \bar{u}}{\partial t} + \bar{u}^2\left(1+\frac{u'}{\bar{u}}\right)\frac{\partial\left(1+\frac{u'}{\bar{u}}\right)}{\partial x} + \bar{u}\left(1+\frac{u'}{\bar{u}}\right)^2\frac{\partial \bar{u}}{\partial x} + \frac{\gamma\bar{p}}{\bar{\rho}\left(1+\frac{\rho'}{\bar{\rho}}\right)}\frac{\partial\left(1+\frac{p'}{\gamma\bar{p}}\right)}{\partial x} + \frac{\left(1+\frac{p'}{\gamma\bar{p}}\right)}{\bar{\rho}\left(1+\frac{\rho'}{\bar{\rho}}\right)}\frac{\partial \bar{p}}{\partial x} = 0$$

Developing the previous equation gives:

$$u\frac{\partial\left(1+\frac{u'}{u}\right)}{\partial t} + \left(1+\frac{u'}{u}\right)\frac{\partial u}{\partial t} + u^2\left(1+\frac{u'}{u}\right)\frac{\partial\left(1+\frac{u'}{u}\right)}{\partial x} + u\left(1+\frac{u'}{u}\right)^2\frac{\partial u}{\partial x} + \frac{\gamma p}{\rho\left(1+\frac{\rho'}{\rho}\right)}\frac{\partial\left(1+\frac{p'}{\gamma p}\right)}{\partial x} + \frac{\left(1+\frac{p'}{\gamma p}\right)}{\rho\left(1+\frac{\rho'}{\rho}\right)}\frac{\partial p}{\partial x} = 0$$

By developing those terms to first order using $\frac{1}{1+\alpha} \simeq 1-\alpha$, neglecting second order terms and temporal derivative of the mean flow and using $c^2 = \frac{\gamma p}{\rho}$ plus Equation 2.2.8 leads to,

$$\bar{u}\left(\frac{\partial}{\partial t} + u^2\frac{\partial}{\partial x}\right)\left(\frac{u'}{\bar{u}}\right) + c^2\frac{\partial}{\partial x}\left(\frac{p'}{\gamma p}\right) + 2u'\frac{\partial \bar{u}}{\partial x} - \bar{u}(\gamma-1)\left(\frac{p'}{\gamma p}\right)\frac{d\bar{u}}{dx} = \bar{u}\frac{s'}{c_p}\frac{du}{dx}$$
$$\Leftrightarrow \left(\frac{\partial}{\partial t} + \bar{u}\frac{\partial}{\partial x}\right)\left(\frac{u'}{\bar{u}}\right) + \frac{c^2}{\bar{u}}\frac{\partial}{\partial x}\left(\frac{p'}{\gamma p}\right) + \left[2\frac{u'}{\bar{u}} - (\gamma-1)\left(\frac{p'}{\gamma p}\right)\right]\frac{d\bar{u}}{dx} = \frac{s'}{c_p}\frac{d\bar{u}}{dx}$$

A.6 Entropy perturbation Equation 2.2.7

Starting with the second principle of thermodynamic:

$$dh = Tds + \frac{dP}{\rho}$$

Assuming an isentropic process so s = Cst $\Rightarrow$ ds = 0 in the previous equation:

$$dh = \frac{dP}{\rho}$$

Moreover, one can also write:

$$du = Tds - Pd\frac{1}{\rho}$$
$$ds = \frac{du}{T} + \frac{P}{T}\frac{1}{\rho}$$

but $du = c_v\ dT$ and $dh = c_p\ dT$ so:

$$ds = c_v\frac{dT}{T} - r\frac{d\rho}{\rho}$$

where dT/T = dP/P-dρ/ρ,

$$ds = c_v\frac{dP}{P} - (c_v + r)\frac{d\rho}{\rho}$$
$$ds = c_v\frac{dP}{P} - c_p\frac{d\rho}{\rho}$$
$$ds = c_v\left(\frac{dP}{P} - \gamma\frac{d\rho}{\rho}\right) \quad \text{where } \gamma = \frac{c_p}{c_v}$$

Thus:

$$\frac{s'}{c_p} = \frac{P'}{\gamma P} - \frac{\rho'}{\rho}$$

A.7 Fractional mass variation Equation 2.2.13

The mass conservation equation is:

$$m = \rho u A$$

With the differencial logarithmic, this equation becomes:

$$\begin{aligned}
\frac{m'}{m} &= \frac{\rho'}{\rho} + \frac{u'}{u} \\
\frac{m'}{m} &= \frac{\rho'}{\rho} + \frac{1}{c}\frac{c}{u}u' \; where \; 1/M = c/u \\
\frac{m'}{m} &= \frac{\rho'}{\rho} + \frac{1}{M}\frac{u'}{c}
\end{aligned}$$

A.8 Fractional variation of stagnation temperature Equation 2.2.15

Starting from the total temperature equation and the prefect gas law,

$$T_t = T\left(1 + \frac{\gamma - 1}{2}M^2\right)$$

Taking the logarithm of the previous equation gives,

$$\ln T_t = \ln T + \ln\left(1 + \frac{\gamma - 1}{2}M^2\right) \tag{A.8.1}$$

$$p = \rho R T$$

differentiating the equation assuming R=constant,

$$\ln p - \ln(\rho R T) = \text{constant}, \tag{A.8.2}$$

$$\frac{dT}{T} = \frac{dp}{p} - \frac{d\rho}{\rho} \tag{A.8.3}$$

differentiating Equation A.8.1 gives,

$$\frac{dT_t}{T_t} = \frac{dT}{T} + \frac{\frac{\gamma - 1}{2}2M dM}{1 + \frac{\gamma - 1}{2}M^2} \tag{A.8.4}$$

but

$$\begin{aligned}
M &= \frac{u}{c}(1 + \frac{u'}{u}) \\
\Rightarrow dM &= \frac{du'}{c} - \frac{u\ dc}{c^2}
\end{aligned}$$

injecting the previous equation in Equation A.8.4 gives:

$$\frac{dT_t}{T_t} = \frac{1}{1 + \frac{\gamma - 1}{2}M^2}\left[\left(1 + \frac{\gamma - 1}{2}M^2\right)\frac{dT}{T} + (\gamma - 1)M\frac{du'}{c} - (\gamma - 1)M\frac{u\ dc}{c^2}\right] \tag{A.8.5}$$

$$\Rightarrow \frac{dT_t}{T_t} = \frac{1}{1 + \frac{\gamma - 1}{2}M^2}\left[\left(1 + \frac{\gamma - 1}{2}M^2\right)\frac{dT}{T} + (\gamma - 1)M\frac{du'}{c} - (\gamma - 1)M^2\frac{dc}{c}\right] \tag{A.8.6}$$

but,

$$c = \sqrt{\gamma RT}$$
$$dc = \frac{1}{2}\frac{\gamma R dT}{\sqrt{\gamma RT}}$$
$$\Rightarrow \frac{dc}{c} = \frac{dT}{2T}$$

Equation A.8.6 becomes:

$$\frac{dT_t}{T_t} = \frac{1}{1+\frac{\gamma-1}{2}M^2}\left[\left(1+\frac{\gamma-1}{2}M^2\right)\frac{dT}{T} + (\gamma-1)M\frac{du'}{c} - (\gamma-1)M^2\frac{dT}{2T}\right] \tag{A.8.7}$$

$$\Rightarrow \frac{dT_t}{T_t} = \frac{1}{1+\frac{\gamma-1}{2}M^2}\left[\frac{dT}{T} + (\gamma-1)M\frac{du'}{c}\right] \tag{A.8.8}$$

Using Equation A.8.3 in Equation A.8.8

$$\frac{dT_t}{T_t} = \frac{1}{1+\frac{\gamma-1}{2}M^2}\left[\frac{dp}{p} - \frac{d\rho}{\rho} + (\gamma-1)M\frac{du'}{c}\right] \tag{A.8.9}$$

$$\Rightarrow \frac{dT_t}{T_t} = \frac{1}{1+\frac{\gamma-1}{2}M^2}\left[\gamma\frac{dp'}{\gamma p} - \frac{d\rho'}{\rho} + (\gamma-1)M\frac{du'}{c}\right] \tag{A.8.10}$$

Equation A.8.10 can be rewritten since the perturbations are small as:

$$\frac{T'}{T} = \frac{1}{1+\frac{\gamma-1}{2}M^2}\left[\gamma\left(\frac{p'}{\gamma p}\right) - \frac{\rho'}{\rho} + (\gamma-1)M\frac{u'}{c}\right]$$

A.9 P_1^- Equation 2.2.19

Using the general solution of the acoustic disturbance 2.2.9, 2.2.11 and Equation 2.2.17 with $P_1^+ = U_1^+ = \varepsilon$ and $\sigma \equiv 0$ (or $\frac{\rho'}{\rho} = \frac{p'}{\gamma p}$) and evaluating $\frac{u'}{c_1}$ and $\frac{p'}{\gamma p_1}$ at $x = 0$.

$$\frac{u'}{c_1} - \frac{\gamma}{2}M\left(\frac{p'}{\gamma p_1}\right) + \frac{1}{2}M\frac{\rho'}{\rho} = 0$$
$$\frac{u'}{c_1} - \frac{\gamma}{2}M\left(\frac{p'}{\gamma p_1}\right) + \frac{1}{2}M\left(\frac{p'}{\gamma p}\right) = 0$$
$$\frac{u'}{c_1} + \frac{M}{2}(1-\gamma)\left(\frac{p'}{\gamma p_1}\right) = 0$$
$$P_1^+ exp(i\omega t) - P_1^- exp(i\omega t) + \frac{M}{2}(1-\gamma)(P_1^+ exp(i\omega t) + P_1^- exp(i\omega t)) = 0$$
$$\Leftrightarrow P_1^+ - P_1^- + \frac{M}{2}(1-\gamma)(P_1^+ + P_1^-) = 0$$

and replacing P_1^+=ε thus finally:

$$P_1^- = \left[\frac{\left(1-\frac{1}{2}(\gamma-1)M_1\right)}{\left(1+\frac{1}{2}(\gamma-1)M_1\right)}\right]\varepsilon$$

A.10 Pressure fluctuation at 0^+ Equation 2.2.20

The harmonic pressure is written:

$$\frac{p'}{\gamma p} = P^+ exp(i\omega[t-\frac{x}{u+c}]) + P^- exp(i\omega[t-\frac{x}{u-c}]) \quad \text{(A.10.1)}$$

and the reflected wave upstream becomes:

$$P_1^- = \left[\frac{\left(1-\frac{1}{2}(\gamma-1)M_1\right)}{\left(1+\frac{1}{2}(\gamma-1)M_1\right)}\right]\varepsilon$$

Assuming and $\frac{p'}{\gamma p} = Cst$ and thus $\frac{p'}{\gamma p_1}(0_-,t) = \frac{p'}{\gamma p_2}(0_+,t)$ to A.10.1 gives:

$$\frac{p'}{\gamma p_1}(0_-,t) = P_1^+ exp(i\omega t) + P_1^- exp(i\omega t)$$

with Equation 2.2.19:

$$\frac{p'}{\gamma p_1}(0_-,t) = \varepsilon exp(i\omega t) + \varepsilon exp(i\omega t)(\frac{1-\frac{(\gamma-1)}{2}M_1}{1+\frac{\gamma-1}{2}M_1})$$
$$\frac{p'}{\gamma p_1}(0_-,t) = \frac{2}{1+\frac{\gamma-1}{2}M_1}\varepsilon exp(i\omega t)$$
$$\frac{p^+}{\gamma p_2}(0_+,t) = \frac{2}{1+\frac{\gamma-1}{2}M_1}\varepsilon exp(i\omega t)$$

A.11 P_2^+ Equation 2.2.21 and P_2^- Equation 2.2.22

Starting with the harmonic pressure 2.2.9, the velocity 2.2.10, the Equation 2.2.17 take the form:

$$\frac{p'}{\gamma p} = P^+ exp(i\omega[t-\frac{x}{u+c}]) + P^- exp(i\omega[t-\frac{x}{u-c}]) \quad \text{(A.11.1)}$$
$$\frac{u'}{c} = P^+ exp(i\omega[t-\frac{x}{u+c}]) - P^- exp(i\omega[t-\frac{x}{u-c}]) \quad \text{(A.11.2)}$$
$$0 = \frac{u'}{c} - \frac{\gamma M}{2}(\frac{p'}{\gamma p}) + \frac{M}{2}\frac{\rho'}{\rho} \quad \text{(A.11.3)}$$

The flow is isentropic so:

$$\frac{p'}{\gamma p} = \frac{\rho'}{\rho}$$

The flow through the nozzle is considered as a discontinuity so the Equation 2.2.17 becomes:

$$\begin{aligned} 0 &= P_2^+ e^{i\omega t} - P_2^- e^{i\omega t} - \frac{\gamma}{2} M_2 (P_2^+ e^{i\omega t} + P_2^- e^{i\omega t}) + \frac{1}{2} M_2 (P_2^+ e^{i\omega t} + P_2^- e^{i\omega t}) \\ 0 &= P_2^+ - P_2^- - \frac{\gamma+1}{2} M_2 (P_2^+ + P_2^-) \\ P_2^- &= P_2^+ \frac{1 - \frac{\gamma-1}{2} M_2}{1 + \frac{\gamma-1}{2} M_2} \end{aligned}$$

Moreover, with the Equations in the previous section:

$$\begin{aligned} \frac{p^+}{\gamma p_2}(0_+, t) &= \frac{2}{1 + \frac{\gamma-1}{2} M_1} \varepsilon exp(i\omega t) \\ \frac{p^+}{\gamma p_2}(0_+, t) &= P_2^+ exp(i\omega t) + P_2^- exp(i\omega t) \\ \text{so}: P_2^+ + P_2^- &= \frac{2}{1 + \frac{\gamma-1}{2} M_1} \varepsilon exp(i\omega t) \end{aligned}$$

Finally combining those Equations where $\varepsilon = P_1^+$ gives:

$$\begin{aligned} P_2^+ &= \left[\frac{1 + \frac{1}{2}(\gamma-1) M_2}{1 + \frac{1}{2}(\gamma-1) M_1} \right] \varepsilon \\ P_2^- &= \left[\frac{1 - \frac{1}{2}(\gamma-1) M_2}{1 + \frac{1}{2}(\gamma-1) M_1} \right] \varepsilon \end{aligned}$$

A.12 P_1^- Equation 2.2.23

Starting with the harmonic pressure 2.2.9, the velocity 2.2.10, the Equation 2.2.17 take the form:

$$\begin{aligned} \frac{p'}{\gamma p} &= P^+ exp(i\omega[t - \frac{x}{u+c}]) + P^- exp(i\omega[t - \frac{x}{u-c}]) \\ \frac{u'}{c} &= P^+ exp(i\omega[t - \frac{x}{u+c}]) - P^- exp(i\omega[t - \frac{x}{u-c}]) \\ 0 &= \frac{u'}{c} - \frac{\gamma M}{2} (\frac{p'}{\gamma p}) + \frac{M}{2} \frac{\rho'}{\rho} \end{aligned}$$

The flow is entropic so:

$$\frac{p'}{\gamma p} = \frac{\rho'}{\rho} + \frac{s'}{c_p}$$

Assuming $P_1^+ = 0$, the Equation 2.2.17 becomes:

$$\begin{aligned} 0 &= -P_1^- - \frac{\gamma}{2} M_1 (P_1^-) + \frac{1}{2} M_1 (P_1^- - \sigma) \\ \frac{-M_1}{2} \sigma &= P_1^- (1 + \frac{\gamma}{2} M_1 - \frac{1}{2} M_1) \\ P_1^- &= \frac{-M_1}{1 + \frac{M_1}{2}(\gamma-1)} \frac{\sigma}{2} \end{aligned}$$

where σ is the fractional temperature.

B One dimensional isentropic perfect gas flow in a variable section duct

A file called *charme_impf*.0 was used as an initial solution in CEDRE code. The field (see Figure 5.3.1) contained in this file is generated using the following hypothesis:

- An quasi-unidimensional flow .
- No heat added to the system ($\delta Q = 0$).
- No work ($\delta W = 0$).
- No friction on the walls.
- No volume forces.
- Isentropic flow.

Under those hypothesis, the resolved equations will be now described.
Starting from the equation of state for an ideal gas:

$$p = \rho r T \tag{B.0.1}$$

and also:

$$h = c_p T \tag{B.0.2}$$

For an isentropic perfect gas flow, one can write:

$$\frac{p}{\rho^2} = constant \tag{B.0.3}$$

using the Equation B.0.1 in the previous Equation gives:

$$\frac{p}{T^{\gamma/(\gamma-1)}} \tag{B.0.4}$$

The sound speed is defined as:

$$c^2 = \left(\frac{\partial p}{\partial \rho}\right)_s = \gamma \rho^{\gamma-1} e^{s/c_v} = \frac{\gamma p}{\rho} = \gamma r T \tag{B.0.5}$$

The goal is now to express all the previous equations using only the Mach number and the isentropic stop conditions. The energy equation for adiabatic flow is defined as:

$$h_i = h + \frac{v^2}{2} \tag{B.0.6}$$

using the fact that $h_i = c_p T_i$, $h = c_p T$ and divide by $c_p T$ the previous result gives:

$$\frac{T_i}{T} = 1 + \frac{v^2}{2 c_p T} \tag{B.0.7}$$

but

$$\frac{v^2}{2c_pT} = \frac{v^2}{2\frac{\gamma r}{\gamma - 1}T} = \frac{\gamma - 1}{2}\frac{v^2}{c^2} = \frac{\gamma - 1}{2}M^2 \tag{B.0.8}$$

thus

$$\frac{T_i}{T} = 1 + \frac{\gamma - 1}{2}M^2$$

Two other expressions can be obtained using the isentropic relation Equation B.0.3:

$$\frac{p_i}{p} = \left(\frac{T_i}{T}\right)^{\frac{\gamma}{\gamma-1}} = \left(1 + \frac{\gamma - 1}{2}M^2\right)^{\frac{\gamma}{\gamma-1}} \tag{B.0.9}$$

$$\frac{\rho_i}{\rho} = \left(\frac{T_i}{T}\right)^{\frac{1}{\gamma-1}} = \left(1 + \frac{\gamma - 1}{2}M^2\right)^{\frac{1}{\gamma-1}} \tag{B.0.10}$$

The temperature (T_i) and the pressure (P_i) stop conditions are constant for an isentropic flow, it is useful to express the mass flow as a function of T_i, P_i, the sectional area and the local Mach number. Starting from the mass conservation equation defined as:

$$\dot{m} = \rho A v \tag{B.0.11}$$

substituting Equation B.0.1 and $v = Mc = M(\gamma r T)^{1/2}$, the previous equation becomes:

$$\dot{m} = \frac{p}{rT}AM(\gamma r T)^{\frac{1}{2}} = AMp(\frac{\gamma}{rT})^{\frac{1}{2}} \tag{B.0.12}$$

using the pressure and the temperature isentropic stop conditions gives:

$$\dot{m} = AMp_i(\frac{p}{p_i})(\frac{\gamma}{rT_i})^{\frac{1}{2}}(\frac{T_i}{T})^{\frac{1}{2}} = AMp_i(\frac{p}{p_i})(\frac{\gamma}{rT_i})^{\frac{1}{2}}(1 + \frac{\gamma - 1}{2}M^2)^{-\frac{(\gamma+1)}{2(\gamma-1)}} \tag{B.0.13}$$

Finally it is relevant to express the ratio between the local section and the critical section $(\frac{A}{A_*})$ as a function of the Mach number. At the critical section A_*, the Mach number is equal to 1 and the mass flow can be defined as:

$$\dot{m}_* = A_* p_i(\frac{p}{p_i})(\frac{\gamma}{rT_i})^{\frac{1}{2}}(1 + \frac{\gamma - 1}{2}M^2)^{-\frac{(\gamma+1)}{2(\gamma-1)}} \tag{B.0.14}$$

and assuming the mass flow conservation $\dot{m} = \dot{m}_*$ gives :

$$\frac{A}{A_*} = \frac{1}{M}\left[\frac{2}{\gamma + 1}(1 + \frac{\gamma - 1}{2})M^2\right]^{\frac{\gamma+1}{2(\gamma-1)}} \tag{B.0.15}$$

Using all the given equations will provided the desired filed for a one dimensional isentropic perfect gas flow in a variable section duct.

C Forcing methods

Non reflecting boundary conditions are based on the decomposition of the flow of characteristic waves leaving or entering the domain proposed by Poinsot *et* al. [39]. Poinsot *et* al. demonstrated for an

one-dimensional flow only three characteristic waves are present see Figure C.0.1. The concerned wave equations are:

$$L_1 = (u - c)\left(\frac{\partial p}{\partial x} - \rho c \frac{\partial u}{\partial x}\right) \tag{C.0.1}$$

$$L_2 = u\left(c^2 \frac{\partial \rho}{\partial x} - \frac{\partial p}{\partial x}\right) \tag{C.0.2}$$

$$L_5 = (u + c)\left(\frac{\partial p}{\partial x} + \rho c \frac{\partial u}{\partial x}\right) \tag{C.0.3}$$

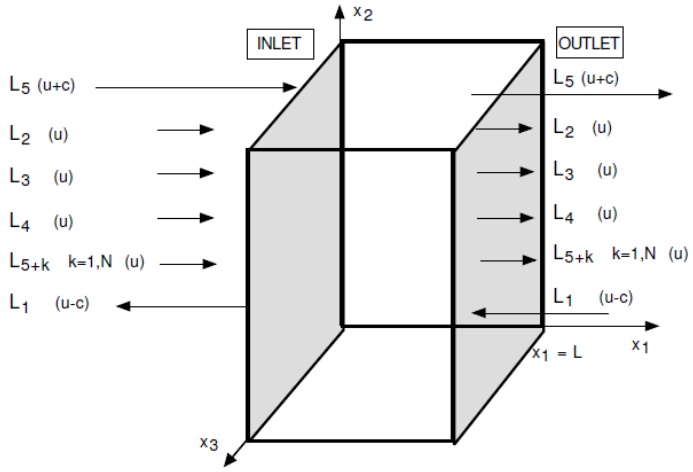

Figure C.0.1: *Boundary conditions located on the x_1 axis [39].*

where L_1 and L_5 define the sound waves moving in the negative and positive x_1 directions respectively and L_2 is the entropy wave L_3 and L_4 are the amplitudes of characteristic waves associated with vorticity and L_{5+k} is the amplitude of characteristic wave of the reacting species. Hence it is possible to inject entropy perturbation or acoustic perturbation. In our case, only the entropy injection will be explained. If one injects only entropy fluctuations, there is no pressure fluctuation meaning that $L_1 = L_5 = 0$. The only equation remaining is the entropy equation, this equation is defined as:

$$L_2 = \frac{\rho c^2}{T}\left[\frac{\partial T'}{\partial t} + (\gamma - 1)\frac{Tu}{A}\frac{dA}{dx}\right] \tag{C.0.4}$$

This relation links directly the temperature fluctuation and the characteristic wave L_2.

D Filtering method

In this study, the focus is on acoustic identities of an entropic wave fluctuation passing a compact nozzle in the subsonic case. As mentioned in 2.2.1, Marble & Candel [31] model gives a prediction of the transfer function of the acoustic wave generation through the passage of an entropic fluctuation in a nozzle which are Equation 2.2.29 and Equation 2.2.30.

Those transfer functions are based on a transfer between three fluctuations modes proposed by Chu & Kovasznay [14] which are:

- An acoustic mode where pressure and velocity fluctuations propagate at the speed of sound.
- A turbulent mode where the pressure and velocity fluctuations are convected at the fluid speed.
- An entropic mode where entropic fluctuations are convected at the fluid velocity.

One can remark that some interactions between those three modes can occur. Thus, the indirect combustion noise can be seen as an interaction between the acoustic and the entropic mode.

The space averaged acoustic variables considered can be decomposed as a sum of three mean quantities (acoustic, turbulent and entropic). Introducing $\langle P \rangle$, the one-dimensional spatial averaged pressure at a point 1, one can write:

$$\langle P_1 \rangle(t) = \langle P_{1acous} \rangle(t) + \langle P_{1turb} \rangle(t) + \langle P_{1entro} \rangle(t)$$

In order to find $\langle P_{1acous} \rangle(t)$, let us consider the acoustic propagation of a one-dimensional wave. If Δt_{12} is the time needed for the wave from 1 to reach the point called 2. Two equations can be written:

$$\begin{aligned} \langle P_1 \rangle(t) &= \langle P_{1acous} \rangle(t) + \langle P_{1r} \rangle(t) \\ \langle P_2 \rangle(t + \Delta t_{12acou}) &= \langle P_{1acous} \rangle(t) + \langle P_{2r} \rangle(t + \Delta t_{12acou}) \end{aligned}$$

where $\langle P_{1r} \rangle(t)$ is the non acoustic part.

Those two equations show that without any dissipation, after the time Δt_{12}, the acoustic wave at position 2 is the same as in 1. This is not valid for the turbulent or the entropic waves which are not necessarily correlated. Based on Kopitz [25] studies, the acoustic filtering method used the propagating characteristic of the acoustic information at a specific speed to filter the non acoustic one (defined as $\langle P_{1r} \rangle(t)$, $\langle P_{2r} \rangle(t)$ and so on). Regarding this, one can write for n points:

$$\begin{aligned} \langle P_1 \rangle(t) &= \langle P_{1acous} \rangle(t) + \langle P_{1r} \rangle(t) \\ \langle P_2 \rangle(t + \Delta t_{12acou}) &= \langle P_{1acous} \rangle(t) + \langle P_{2r} \rangle(t + \Delta t_{12acou}) \\ \langle P_3 \rangle(t + \Delta t_{12acou} + \Delta t_{23acou}) &= \langle P_{1acous} \rangle(t) + \langle P_{3r} \rangle(t + \Delta t_{12acou} + \Delta t_{23acou}) \\ \vdots &= \vdots \\ \langle P_n \rangle(t + \Delta t_{12acou} + \cdots + \Delta t_{(n-1)nacou}) &= \langle P_{1acous} \rangle(t) + \langle P_{nr} \rangle(t + \Delta t_{12acou} + \cdots + \Delta t_{(n-1)nacou}) \end{aligned}$$

Summing all the terms on the left hand side and in the right hand side gives:

$$\sum_{i=1}^{n} \langle P_i \rangle(t + \sum_{j=1}^{i} \Delta t_{(j-1)jacou}) = n \langle P_{1acous} \rangle(t) + \sum_{i=1}^{n} \langle P_{ir} \rangle(t + \sum_{j=1}^{i} \Delta t_{(j-1)jacou})$$

assuming $\Delta t_{01acou} = 0$

The last term in the right hand side goes to zero when n is becoming larger, the reason is that this term is a sum of different phase shift waves amplitudes to each other and with random phase angle difference. Thus with $\sum_{i=1}^{n} \langle P_{ir} \rangle(t + \sum_{j=1}^{i} \Delta t_{(j-1)jacou}) \sim 0$, one can write:

$$\langle P_{1acous} \rangle(t) \approx \frac{\sum_{i=1}^{n} \langle P_i \rangle(t + \sum_{j=1}^{i} \Delta t_{(j-1)jacou})}{n}$$

When the wave is propagating in the positive x-direction denotes as P^+, the acoustic propagation speed is defined as $u + c$, where u is the local fluid speed and c is the local speed of sound. In the same idea, the wave is propagating in the negative x-direction denotes as P^-, the acoustic propagation speed is defined by $\mid u - c \mid$. This wave is interesting as it will give the amplitude of the reflected waves through the nozzle. The times Δt^+ and Δt^-, where $+$ denotes the positive x-direction and $-$ denotes the negative x-direction, can now be defined by:

$$\Delta t^+_{(j-1)j} = \frac{D_{(j-1)j}}{V_{(j-1)j}} = \frac{D_{(j-1)j}}{\frac{u_{(j-1)} + u_j}{2} + \frac{c_{(j-1)} + c_j}{2}} \tag{D.0.1}$$

$$\Delta t^-_{(j-1)j} = \frac{D_{(j-1)j}}{V_{(j-1)j}} = \frac{D_{(j-1)j}}{-\frac{u_{(j-1)} + u_j}{2} + \frac{c_{(j-1)} + c_j}{2}} \tag{D.0.2}$$

Where $D_{(j-1)j}$ is the distance between the point $j-1$ and j and using the assumption that the acoustic propagation speed is the average of the propagating speed at $j-1$ and j.